cambridge.org/aog

Particle tracking in snow avalanches with *in situ* calibrated inertial measurement units

Robert Winkler[1] iD, Michael Neuhauser[2] iD, Rene Neurauter[3] iD, Felix Erlacher[4] iD, Walter Steinkogler[5],* iD and Jan-Thomas Fischer[2] iD

[1]Department of Engineering & IT, Carinthia University of Applied Sciences, Villach, Austria; [2]Department of Natural Hazards, Austrian Research Centre for Forests (BFW), Rennweg 1, Innsbruck, Austria; [3]Department of Mechatronics, University of Innsbruck, Techniker Straße 13, Innsbruck, Austria; [4]Cancom a+d, Innsbruck, Austria and [5]Wyssen Avalanche Control, Reichenbach, Switzerland

Abstract

In the course of an artificially triggered avalanche, a particle tracking procedure is combined with supplementary measurements, including Global Navigation Satellite System (GNSS) positioning, terrestrial laser scanning and Doppler radar measurements. Specifically, an intertial measurement unit is mounted inside a rigid sphere, which is placed in the avalanche track. The sphere is entrained by the moving snow, recording translational accelerations, angular velocities and the flux density of Earth's magnetic field. Based on the recorded data, we present a threefold analysis: (i) a qualitative data interpretation, identifying different particle motion phases which are associated with corresponding flow regimes, (ii) a quantitative time integration algorithm, determining the corresponding particle trajectory and associated velocities on the basis of standard sensor calibration, and (iii) an improved quantitative evaluation relying on a novel in situ sensor calibration technique, which is motivated by the limitations of the given dataset. The final results, i.e. the evolution of the angular orientation of the sensor unit, translational and rotational velocities and estimates of the sensor trajectory, are assessed with respect to their reliability and relevance for avalanche dynamics as well as for future design of experiments.

1. Introduction

Gravitational mass flows in general appear in different forms, ranging from continuum motion such as fluvial processes to particle governed motion like rock falls. Snow avalanches in particular show various flow types including dense basal flow of snow granules or destructive powder snow flows (Sovilla and others, 2014; Köhler and others, 2018a), going beyond the powder/dense flow avalanche dichotomy (Faug and others, 2018). Experiments to access flow dynamics at the particle level have been limited to the analysis of avalanche deposits (Bartelt and McArdell, 2009) or to laboratory experiments that reveal interesting details on the granular behaviour (Steinkogler and others, 2015a) and surprising temperature dependence of snow (Fischer and others, 2018). On a field scale, some of the standard approaches of motion tracking are prone to fail in snow avalanches (e.g. limited visibility for photogrammetry or antenna orientation and signal attenuation by snow for GNSS methods). So far, *in situ* inertial measurements have therefore been limited to chute experiments, providing estimates on speed and position along a predefined chute topography (Vilajosana and others, 2011).

An improved knowledge of internal particle dynamics in snow avalanches is desirable, not only to better understand the governing processes and to acquire data for model evaluation, but also for a reliable prediction of single particle motion. With this information, scientists and engineers may have a new opportunity to identify and interpret impact pressures that cannot directly be examined by classical approaches (Faug, 2015; Sovilla and others, 2016; Kyburz and others, 2022a, 2022b) or to predict the transport and corresponding burial location of avalanche victims. During the past few years, several researchers have developed independently the idea to apply methods of inertial navigation for a motion tracking in gravitational mass movements. Related endeavours aim at reliable motion data including particle velocities, inertial effects (centrifugal forces) and vertical motion relatively to the terrain (due to buoyancy and segregation). The basic idea is to record translational acceleration and angular velocity components, which, in principal, allow to determine a trajectory via time integration. Most recently, the suitability of inertial navigation devices in combination with observations through unmanned aerial vehicles has been investigated for the recording of rockfall trajectories, also providing a review of related approaches (Caviezel and others, 2019). Furthermore, Dost and others (2020) investigated the potential of inertial sensor devices in laboratory landslide experiments, introducing the Smartstone probe v2.0 as a device to measure movement characteristics of single clasts. They highlight how physical movement characteristics can be derived from the measured and calibrated data and the potential of a 2D and 3D visualization of the paths a clast took during the movement and how these visualizations allow for an easy recognition of complex motion patterns. These developments allowed to investigate the influence of shape and mass in rockfall experiments (Caviezel and others, 2021) or in depth motion analysis utilizing rockfall video trajectories (Noël and others, 2022).

Inertial navigation systems are widely used in engineering as well as everyday life applications such as naval, aircraft and, in particular, drone navigation, positioning in cell phone applications and many others. Most modern inertial navigation systems belong to the class of so-called strap-down devices (Groves, 2008). The method of strap-down inertial navigation is based on the measurement of accelerations and angular velocities by means of sensor clusters 'rigidly' linked to a moving object of interest.[1] Corresponding devices are commonly called 'inertial measurement units' (IMU). If earth's magnetic field is detected in addition, the term 'motion processing unit' is preferred by some authors. An extensive overview of accelerometer, gyroscope and magnetometer technology is given in Titterton and Weston (2004).

Position and orientation data are obtained by numerical integration of the kinematic differential equations (navigation equations) relating the time derivatives of position and orientation (angular) parameters with the acceleration and angular velocity components (Groves, 2008). A common approach to improve the accuracy of the integration procedure is to apply stochastic estimation techniques, such as Kalman filtering (Simon, 2006). Such methods rely on a deterministic model predicting the system dynamics, a measurement model and on specific assumptions related to the stochastic properties of the measurement error. For tracking applications, the system as well as the measurement model are non-linear, which leads to complex implementations involving a reasonable number of tuning parameters, a proper adjustment of which is often difficult. However, a beneficial peculiarity of the tracing problem is that the non-linearity originates from the angular motion only and that the related kinematic differential equations can be integrated independently from the state variables of the translational motion.[2] A commonly known algorithm for the estimation of IMU orientation which avoids the complexities of non-linear state estimation has been released by Madgwick and others (2011). The idea is to determine the orientation increment in each time step twice: once via integration of the angular rates and once from magnetometer and/or accelerometer data. The orientation is then updated by a weighted average of both increments. The method works particularly well if no (or only small) inertial accelerations occur, i.e. if the accelerometers measure only the effect of gravity. In this case, the orientation can be determined uniquely from accelerometer and magnetometer data by solving a minimization problem. In the case of avalanche tracking, it turned out that acceleration signals are of limited use for this purpose. As long as only the magnetometer data are available for the orientation estimation, this procedure is not unique. Therefore, a new algorithm has been developed which allows to determine the sensor orientation from gyroscope and magnetometer data in a robust manner even under the rough conditions of the present application. The orientation information at each time step can then be used to transform the acceleration components to a global coordinate system, which, in turn, allows to apply a simple numerical integration scheme for the determination of velocity and position.

One of the first real-scale avalanche particle tracking experiments, which was accompanied by Doppler radar measurements and terrestrial laser scanning (TLS), has been performed at the Flüelapass field site in Switzerland on 23 January 2013. At this time, the experiments focused on infrared thermography and corresponding avalanche temperatures (Steinkogler and others,

2015b). Due to the lack of prior experience, multiple prominent problems arose related to the particle tracking measurement technology applied: Firstly, the sensor calibration has been performed under laboratory conditions that do not sufficiently correspond to the relevant field conditions. Secondly, the measurement range of the gyrometers has been chosen too small, which has lead to a cut-off of angular velocity peaks at about $\pm 360° \, s^{-1}$.[3] Additionally, a technical recording error limits the possibility of a full data integration. However, these limitations inspired the development of corresponding workarounds, which not only allow to deduce the desired results but in addition give rise to novel methods of sensor calibration. These aspects are described in detail below. The main focus of this manuscript is therefore the methodological description of the approaches and numerical procedures, which have been developed to tackle the specific deficiencies of the given dataset. The observed avalanche event provides a test case to assess both, the experimental setup as well as the related methods of data processing. It is emphasized that the present work is dealing with the evaluation of, so to say, 'historical' data, which have been recorded with the help of, from today's point of view, outdated hardware. At the time of the experiment, the combination of procedures presented here was not available, whereas attempts to apply conventional approaches failed. Despite the technological advances of the last years, the availability of comparable data from real-scale experiments is still limited, such that trying to extract as many results as possible even from outdated experiments is justified. Most recent approaches highlight the usability of state-of-the-art hardware, investigating particle motion in avalanches with global tracking (Global Navigation Satellite System [GNSS]) approaches (Neuhauser and others, 2023). The article is organized as follows: Section 2 describes the details of the experimental procedure. It is followed by an overview of the recorded IMU data and a qualitative assessment and interpretation (Section 3). Theory, results and assessment of a quantitative evaluation of the IMU data based on a standard sensor calibration yielding estimates of angular orientation, translational and rotational velocities, as well as the sensor trajectory are given in Section 4. The numerical procedure providing the angular orientation is specifically designed to optimally deal with the given dataset. Motivated by a misalignment of the recovered trajectory, a novel calibration approach is introduced, applied and assessed in Section 5. Sections 6 and 7 summarize and finally assess the findings, discuss their significance for the fields of avalanche research in particular as well as for the problem of motion tracking in general and address the lessons learned for future avalanche experiments. The standard procedures of sensor calibration are briefly summarized and postponed to Appendix A, since they rely on state-of-the-art algorithms. The recovery of deficient gyrometer data is not state-of-the-art but is considered too specific to justify interrupting the flow of argumentation in the main text and is therefore placed in Appendix B.

2. Experimental set-up and test procedure

To investigate the particle movement in a snow avalanche, a measuring device, subsequently also called *sensor unit*, is placed in the release area or potential flow path before the avalanche is triggered. In the course of the experiment the sensor unit is expected to be entrained and further transported by the moving snow and thus to resemble the particle motion in the avalanche. The measuring device consists of several sensors, a micro controller, a data storage unit and an electrical power supply, which are embedded in a rigid, spherical housing (Fig. 1). The housing

---

[1]'Rigidly linked' might include an interconnection of shock or vibration absorbers. It has to be understood as the opposite of a stabilized system mounted in a Cardan suspension.

[2]This holds as long as there are no constraint conditions relating rotational and translational motion.

[3]Note that the observed maximum angular velocity values of about $\pm 360° \, s^{-1}$ are in fact absolutely larger than the *nominal* measurement range of $\pm 300° \, s^{-1}$.
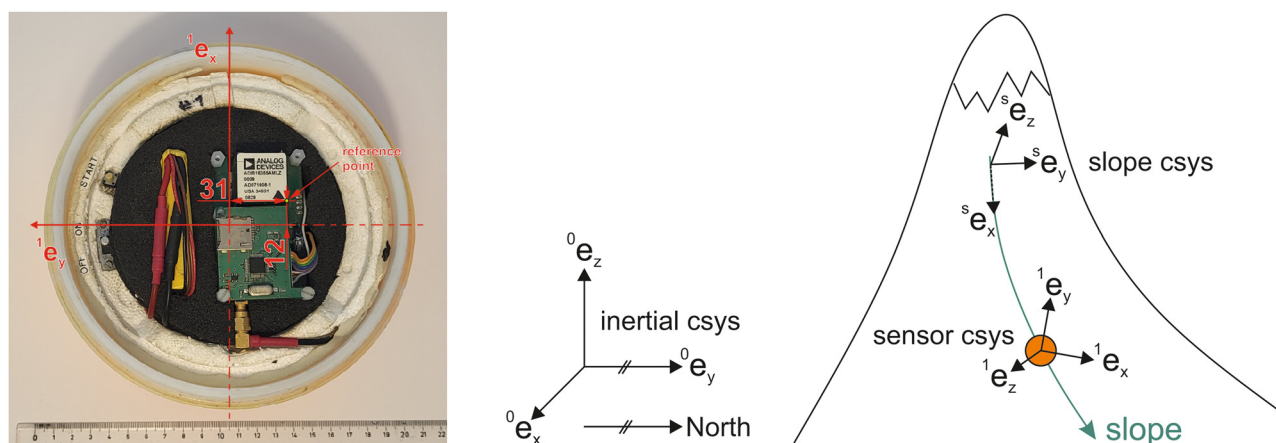
Figure 1. *Left:* Top view of the sensor unit with opened housing. The x and y axes of the sensor coordinate system are drawn at the geometric centre of the spherical casing. The reference point to which the accelerations are referred to coincides with a corner of the bottom face of the cuboidal IMU housing. Its position vector relatively to the drawn coordinate system is $^1\boldsymbol{\varepsilon} \approx [12 \ -31 \ -12]^T$ mm. *Right:* Coordinate systems referred to in this work: inertial, sensor and slope coordinate system (or frame).

properties are chosen to resemble snow granules found in avalanche deposits (Bartelt and McArdell, 2009) with a density of ≈ 300 kg m^{-3} and a diameter of ≈ 16 cm (Fischer and Rammer, 2010). The sensors applied involve a six-axis inertial sensor (IMU), a three-axis magnetometer and a GNSS module. The utilized IMU (ADIS16355) is an assembly of three accelerometers and three gyrometers aligned with three mutually perpendicular directions and capable of measuring the corresponding acceleration and angular velocity components, respectively. The magnetic sensor HMC1043 measures the magnetic flux density[4] in the same directions (nominally). The applied GNSS module is a ublox LEA-4T-0-000 receiver. The power supply is provided by a rechargeable battery. Data are recorded with a sampling rate of 150 Hz and stored on an SD card. The measurement range of gyrometers is set to a nominal value of $\pm 300°$ s^{-1} with a digital resolution of 14 bit and a sensitivity of 0.0725–0.0740° s^{-1} LSB^{-1}. The range of accelerometers is nominally ± 10 g with a digital resolution of 14 bit as well and a sensitivity of 2.471–2.572 mg. The range of magnetometers is nominally ± 6 Gs with a sensitivity of 0.8–1.2 mV V Gs^{-1}. The six inertial sensors (gyrometers and accelerometers) are assembled in a cuboidal housing with an edge size of approximately 23 mm. While the positioning of gyrometers is uncritical[5] the positioning of accelerometers deserves a certain attention: since the three accelerometers cannot be located at the same position, a so-called origin alignment is applied internally by the device, such that the acceleration values refer to a defined reference point. This reference point is depicted in (Fig. 1).

To recover the sensor unit velocity and trajectory from the recorded data (*tracking*), a proper calibration of IMU sensors (including magnetometers) is crucial. An overview of the standard calibration procedures applied here, can be found in Appendix A. Originally, the calibration of the three-axis accelerometer has been done on the basis of a standard six-position static test referring to earth's gravitational acceleration as a reference. To calibrate the three-axis gyrometer, constant angle rate tests have been performed utilizing a Stäubli TX2-90 industrial robot, following the methods, described by Aggarwal and others (2008) or Stančin and Tomažič (2014). The magnetometer calibration is performed applying Earth's magnetic field as a reference

(Renaudin and others, 2010). Retrospectively, it turned out that it is a certain drawback of the experimental work that the calibration procedures have not been performed in temporal and local proximity to the measurements. Since the experiment has been one of the first of its kind, a lack of appropriate experience has thus lead to some effect of misjudgement. In particular, the laboratory calibration of magnetometers proved to be inadequate: measuring Earth's magnetic field provides information about the angular orientation of the sensor unit. To this end it has to be ensured that the magnitude of the measured flux density is basically constant. If this is not the case, either (electro-) magnetic disturbances are present or the calibration of the magnetometers is wrong. Both sources of error would corrupt the evaluation of angular orientation, the knowledge of which is decisive for a proper tracking process. In the present case, an existing non-constancy of the magnetic field could be attributed to the inadequacy of the laboratory calibration and be remedied by a recalibration on the basis of the in-field data. The theoretical background and an assessment of the procedure can be found in Appendix A. The name 'in situ calibration' is suggested for this approach. The laboratory calibration of accelerometers also represents a source of error and can be improved by an in situ approach as well. Section 5 is dedicated to this topic.

The test site is located close to Davos in Switzerland [46.748621°(N), 9.945134°(E), WGS84]. The avalanche path is a north-east facing slope, with an altitude difference of 600 m. Deposits of larger avalanches typically reach a lake located at 2374 m a.s.l. at the bottom of the slope (Fig. 2). The slope angle ranges from 50° in the rock face in the upper part to 20° at the beginning of the run-out zone with an average of 30° of the open slope at around 2600 m a.s.l. The avalanche had an approximate destructive size d2 (Canadian Avalanche Association, 2016) and was released artificially. According to the international avalanche classification (De Quervain, 1981) avalanche 20130123 classifies as A2B4C1D2E2F4G1H1J4, with a possible variation concerning the form of motion (mixed type with powder part, E7).

Supplementary measurements of the avalanche event include video recordings (see supplementary material), Doppler radar measurements, pre-event terrain reconstruction by means of TLS and GNSS positioning of the tip of the avalanche deposition and of the final location of the sensor unit. The Doppler radar observations deliver a range-time diagram of the avalanche front (amongst other information). Roughly speaking, the slope of the range-time curve equals the velocity of the avalanche

---

[4]Sometimes simply called magnetic field, which is, from a physicist's point of view, not correct, but uncritical in the present case.

[5]The angular velocity of a rigid body is independent of the origin of the reference frame (Wittenburg, 2008).
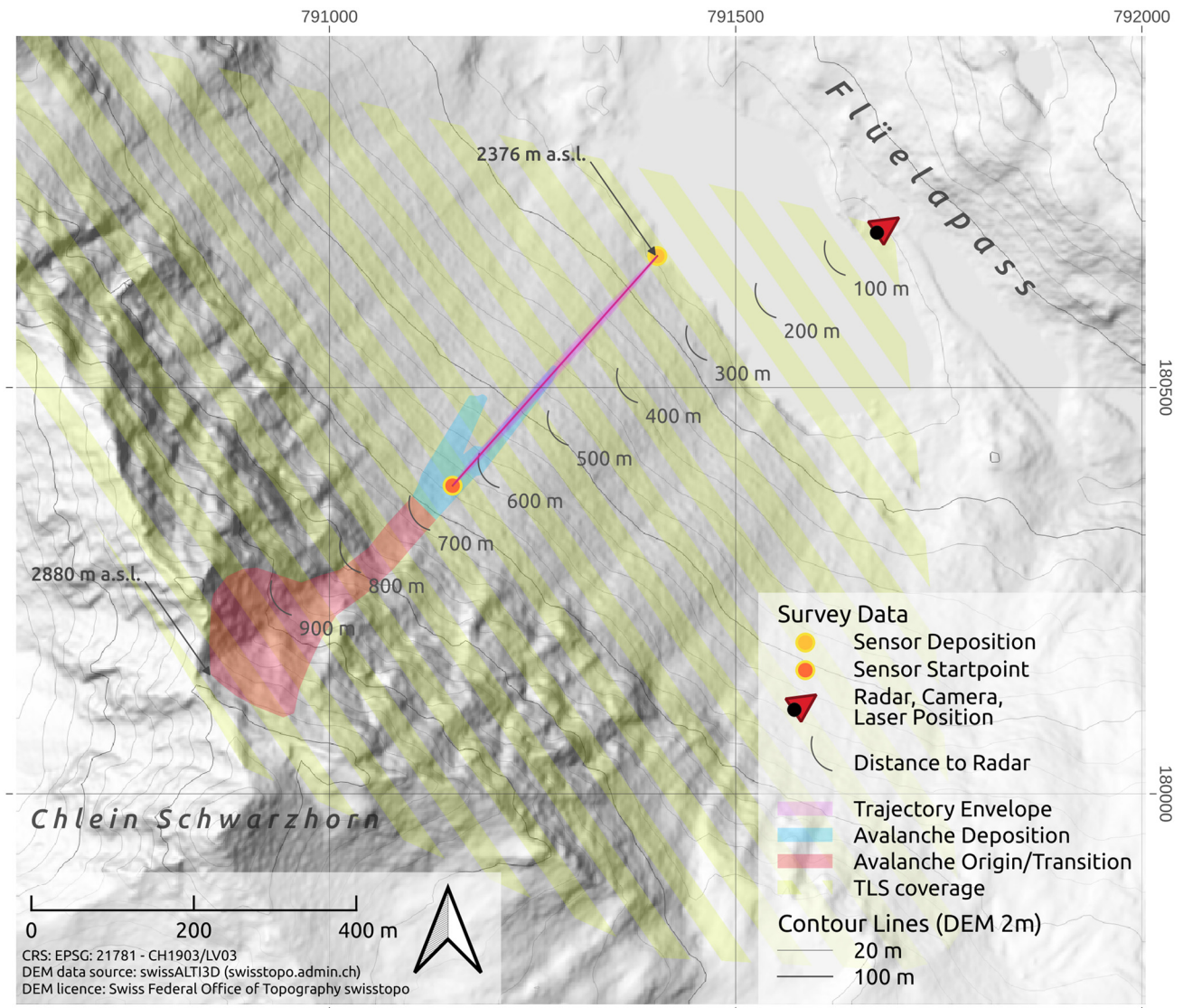
Figure 2. Overview of the test site including the main avalanche release, track and deposit, the sensor unit trajectory, as well as radar, TLS and video camera position with relative, projected distance to the avalanche.

front projected onto the instantaneous radar beam (Gauer and others, 2007; Rammer and others, 2007; Gauer and Kristensen, 2016). To account for the topography, radar velocities are scaled with $1\cos^{-1}\delta$, where δ is the angle between the slope line and the radar beam (Fischer and others, 2014). The range time diagram involving the radar signal strength is presented in Figure 3. Comparing the so obtained frontal velocities with the sensor unit velocity recovered from the IMU data helps to assess the tracking procedure and gives further hints related to the motion of the sensor unit relatively to the avalanche front.

After release, the avalanche quickly accelerated to velocities between 20 and 25 m s^{-1} and developed a small powder part. The main mass movement was characterized by a dense flow and a pronounced roll-wave activity (see Fig. 3 and the supplementary video material), showing the typical characteristics of a cold dense regime as defined in Köhler and others (2018b). The sensor unit has been entrained by the avalanche in the upper part of the open avalanche track with a frontal velocity between 20 and 21 m s^{-1} at an approximate distance of 650–675 m from the radar device. After a steady phase, flow velocities decrease from 18 to 10 m s^{-1}, the main avalanche body came to rest at a radar distance of 450–475 m. Up to this point (about 16 s after being entrained), the sensor unit has covered a travelling distance

of 220–225 m within the dense cold regime and finally detached from the avalanche body. Together with snow fragments, remaining from the entrainment process, the sensor unit kept moving in a rolling motion within the snowball regime (Köhler and others, 2018b). The individual snowballs or snow wheels are visible in radar distances between 250 and 450 m, rolling down the slope with varying velocities between 7 and 13 m s^{-1}. The rolling motion can qualitatively be reconstructed by the sensor data. The total duration of the movement was 70 s and is in accordance to the radar recordings.

The GNSS measurements were used to determine the initial and final sensor unit position with a corresponding trajectory length of $\approx$ 420–430 m. To obtain an estimate of the sensor unit trajectory, a straight line is assumed from the initial to the final sensor unit position, see the purple area depicted in Figure 2. The x (East) and y (North) coordinates of the starting and of the end point are obtained from the data of the GNSS module contained in the sensor housing and are averaged over a time period of several minutes. The coordinates of the tip of the avalanche deposition have been checked with the help of an external GNSS receiver. The orographic left and right boundaries of the trajectory envelope are obtained by projecting the envelope onto the terrain surface given by the TLS terrain model. The
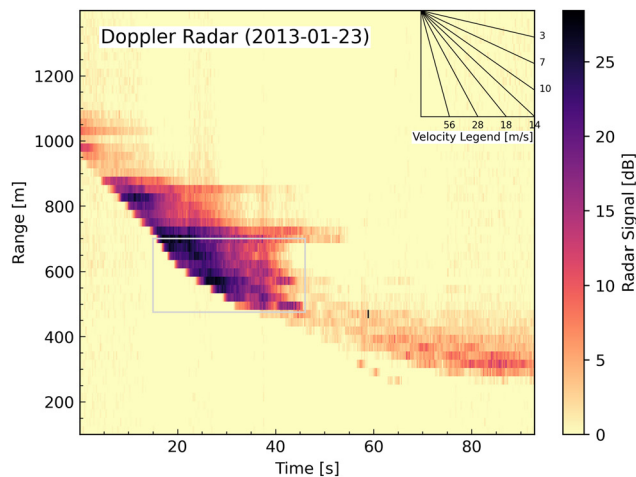
Figure 3. *Left:* Range-time diagram of the Doppler radar measurement, from which the frontal avalanche velocities can be deduced and which allows for the cross-validation of the corresponding flow regimes. The gray framed box indicates the relevant domain related to the present experiment: from entrainment of the sensor unit stillstand of the bulk of the avalanche. The signals below that box refer to individual snowballs moving further for a while. *Right:* The avalanche shortly before the transition from the cold-dense to the snowball regime corresponding to the steady flow phase. The sensor unit (indicated by the red circle) is about to leave the bulk of the avalanche.

diameter of the trajectory envelope is assumed to equal the maximum width of the lower part of the avalanche deposition. The geometry of the terrain surface serves as an input for the in situ calibration and the trajectory envelope is used to assess the trajectory recovered from inertial measurements via the numerical algorithms described in this work. To account for the resolution and the accuracy of the terrain model (±0.5 m, each), the surface projection of the envelope (a rhombus, basically) is extruded (1 m in outward and 1 m in inward normal direction) to become a double wedge and is referred to as *reference tube*.

3. Experimental results and qualitative analysis

3.1. Overview

As already anticipated in the introduction, the measurement process has come along with some shortcomings: Firstly, the occurring angular velocities occasionally exceed the measurement range of the gyrometers and, secondly, a failure of data recording occurred approximately 9 s after the sensor unit has been entrained by the avalanche, such that reliable data are missing over a time span of about 0.5 s. The first problem can be circumvented with the help of magnetometer data. The second one strictly limits any quantitative motion analysis to the time span $[0, 9]$ s. Nevertheless, qualitative conclusions can be drawn from the entire dataset covering the time span from start ($t = 0$ s) to stop ($t \approx 70$ s) of the sensor unit motion.

The detailed analysis of the recorded data is subsequently carried out in three steps:

1. A qualitative motion analysis (this section) on the basis of raw data allows to identify different phases of sensor unit motion. The conclusions drawn are independent of any theoretical assumption and are not affected significantly by the recording failure at $t \approx 9$ s.
2. Quantitative motion analysis (Section 4) on the basis of standard calibration of inertial sensors: in the next section, numerical methods are developed by which means estimates of rotational as well as translational motion within the time span from 0 to 9 s are obtained. The recovered evolution of the angular orientation is plausible, whereas the recovered trajectory significantly deviates from the topography. The quantitative results strongly depend on the sensor calibration.

3. Recalibration of accelerometers (Section 5) based on a topography constraint (in situ calibration) yields an improved trajectory and an improved velocity evolution.

3.2. Identification of motion phases

A qualitative analysis of the recorded IMU data allows to identify the main particle motion phases. The corresponding signals are depicted in Figures 4 and 5. The supplementary video serves as a visual reference.

Phase 0: Sensor unit at rest for time $t < 0$. Acceleration measurements correspond to the gravitational acceleration and allow (together with the magnetic field) to deduce the angular orientation of the sensor unit.

Phase 1: Entrainment at $t = 0$. The sensor unit is captured by the avalanche front and is heavily accelerated until $t \approx 0.6$ s.

Phase 2: Ballistic motion. The sensor unit appears to be catapulted through the air. The measured acceleration signals are almost zero (i.e. inertial and gravitational forces nearly cancel each other) until $t \approx 1.4$ s.

Phase 3: Impact. The sensor unit gets in contact with the dense snow again. Acceleration peak at $t \approx 1.4$ s.

Phase 4: Steady flow. The sensor unit floats with the bulk of moving snow. The acceleration signal is dominated by random variations until $t \approx 15.5$ s. Acceleration peaks indicate that some saltation (sequences of ballistic motion followed by impacts) takes place.

Phase 5: Rolling: The sensor unit leaves the avalanche at $t \approx 15.5$ s and starts to roll downward. The fast-rolling character of the motion can be seen from high spin rates (exceeding the gyrometer measurement range) and from the oscillating behaviour of the magnetic field component (light green curves in Figs 4 and 5). The acceleration signals shift in the negative direction indicating a high centripetal acceleration due to high spin rates. At $t \approx 52$ s the rotational motion starts to slow down continuously and stops at $t \approx 70$ s.

Phase 6: Sensor unit at rest for $t \gtrsim 70$ s

Particle motion phases 1–4 (entrainment, ballistic motion, impact, steady flow) are associated to the cold-dense flow regime,
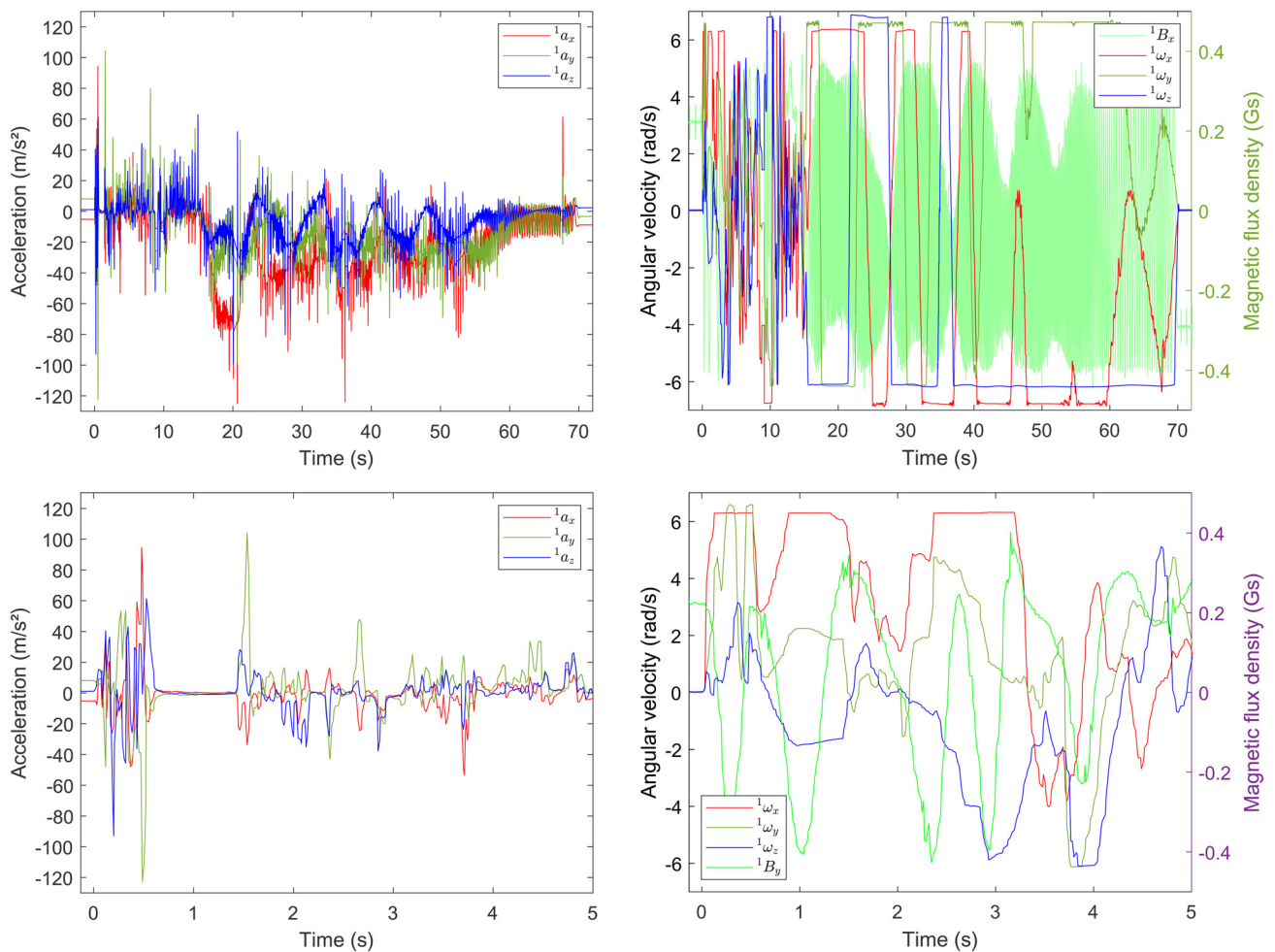
Figure 4. *Top:* Complete sequence of accelerometer (*left*) and gyrometer raw data (*right*) recorded in the course of the avalanche event ($0 \leq t \leq 70$ s). *Bottom:* Motion phases 0–4 (incomplete). As can be seen from the diagrams on the right-hand side, the gyrometers are saturated in a large part of the entire time span. To still be able to derive reliable information about the rotational motion, the local y component of the magnetic field is plotted in addition (light green curve).

with particular emphasis on the initial rapid acceleration, which is associated with the corresponding avalanche velocities. The detachment of the main avalanche body at ≈ 15.5 s and subsequent transition to the snowball regime is represented by phase 5 (rolling) and followed by the final sensor unit deposition (phase 6).

4. Processing of inertial navigation data

4.1. Theory

In principle, IMUs are designed to enable the determination of angular orientation, translational velocity and position. While the reliability of angular orientation is usually high, the one of velocity and, even more, of position suffer from an unavoidable drift occurring in the course of an unavoidable integration procedure (Neurauter and Gerstmayr, 2022). To obtain long-term stable results, additional information is required (GNSS data, e.g.). The Flüela experiment has revealed that the sensor unit in action has been subjected to high and strongly varying rotation rates (with a maximum of about 330 rpm ≈ 35 rad s^{-1} within the first 9 s) and to frequent and randomly distributed acceleration peaks, the strongest of which reaching almost 15 g (≈ 150 m s^{-2}; see Figs 6 and 11). Considering the strongly, almost randomly, varying character of the raw data, it can be concluded that avalanche particle dynamics are dominated by stochastic rather

than deterministic effects. These circumstances indicate that for the determination of velocity and position from the IMU data, standard methods of state estimation (see Crassidis and others, 2007, e.g.) are not well suited. These methods rely on the assumption that the state of a physical system is basically determined by a dynamical model and subjected to stochastic disturbances. While for simple types of motion (moving vehicles, e.g.), such models can be obtained from the trivial assumption of constant translational acceleration and constant angular velocity throughout each time interval, there is presently no concept from which an appropriate dynamical model could be derived for the translational and rotational motion of a particle driven by an avalanche. Therefore, an alternative procedure, subsequently called *tracking algorithm* for the evaluation of avalanche particle dynamics is proposed:

1. The angular orientation of the sensor unit is determined via an adapted integration procedure applied to the gyrometer and magnetometer data
2. At each time step, the corresponding rotation matrix is employed to transform the measured data from the local sensor frame to the global one
3. Velocity and position data are obtained from the global acceleration components via standard time integration (trapezoidal rule)
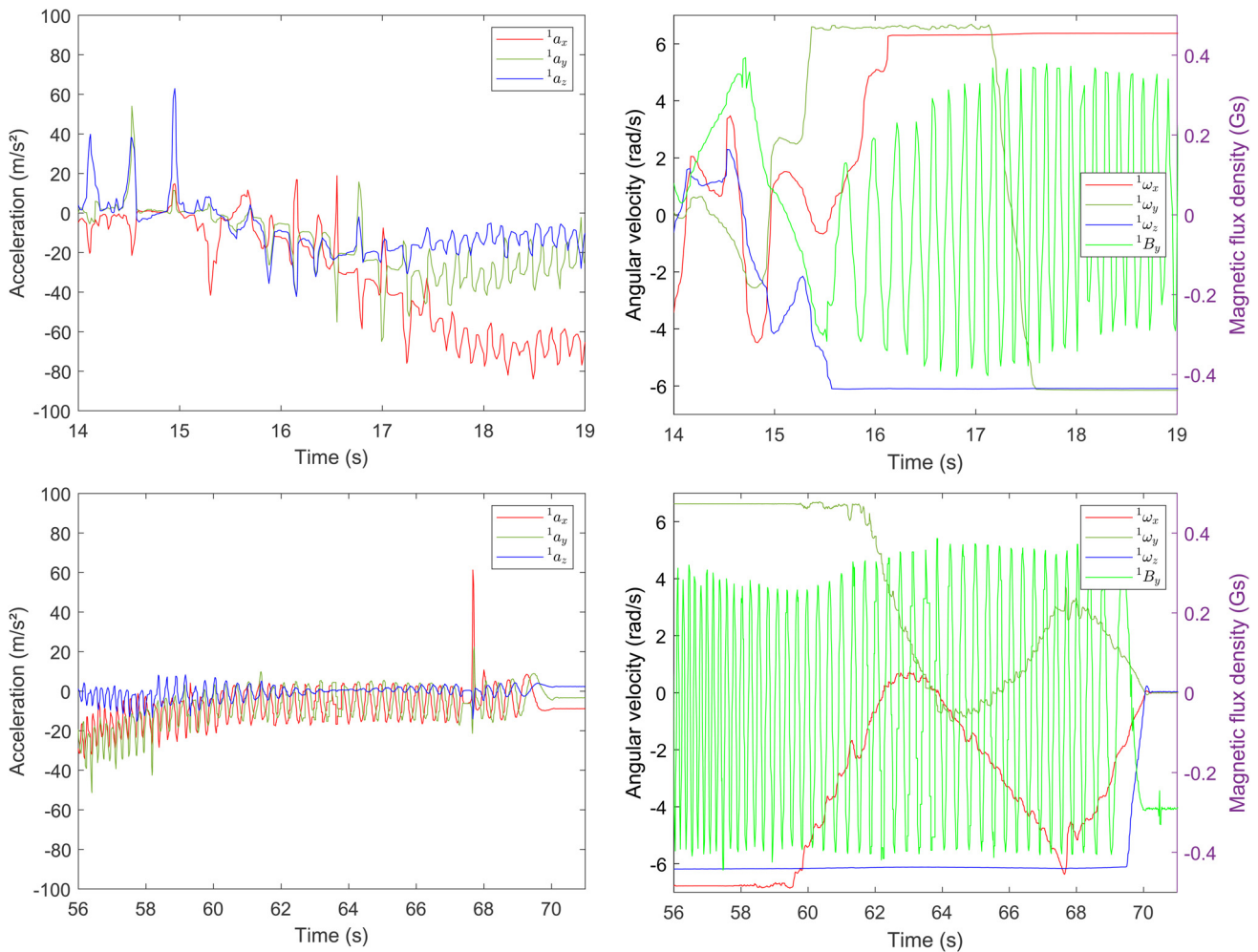
Figure 5. *Top:* Transition from motion phase 4 (steady flow) to phase 5 (rolling). *Bottom:* The final seconds of the rolling phase. The prominent acceleration peak (bottom-left) at $t \approx 67.7$ s comes from an impact at the end of a small hill jump. The statement concerning the gyrometer data in the previous figure also applies here.

4.1.1. Recovery of angular orientation

The tracking algorithm essentially relies on the knowledge of the angular orientation of the sensor system at every time step. The angular orientation at time t is uniquely determined by an orthogonal matrix

$$\mathbf{R}(t) = \begin{bmatrix} \mathbf{e}_x^1(t) & \mathbf{e}_y^1(t) & \mathbf{e}_z^1(t) \end{bmatrix} \tag{1}$$

establishing an active rotation of the inertial (global) coordinate axes ($\mathbf{e}_x^0$, $\mathbf{e}_y^0$, $\mathbf{e}_z^0$) onto the sensor-fixed (local) coordinate frame ($^1\mathbf{e}_x$, $^1\mathbf{e}_y$, $^1\mathbf{e}_z$), see Figure 1. The kinematic differential equation governing the evolution of $\mathbf{R}(t)$ reads (Wittenburg, 2008)

$$\dot{\mathbf{R}}(t) = {}^0\mathbf{\Omega}(t)\,\mathbf{R}(t), \quad \mathbf{R}(0) = \mathbf{R}_0 \tag{2}$$

with

$$^0\mathbf{\Omega} = \begin{bmatrix} 0 & -{}^0\omega_z & {}^0\omega_y \\ {}^0\omega_z & 0 & -{}^0\omega_x \\ -{}^0\omega_y & {}^0\omega_x & 0 \end{bmatrix} \tag{3}$$

being the skew-symmetric 3×3 matrix corresponding to the vector $^0\boldsymbol{\omega} = [\,{}^0\omega_x\ {}^0\omega_y\ {}^0\omega_z\,]^T$ of angular velocity components. To distinguish between vector components related to the corotating sensor frame and those related to the inertial frame, a left-hand superscript index is introduced, with 0 referring to the inertial

and 1 to the corotating frame (compare Fig. 1). Inertial and corotating coordinates are related to each other via a passive rotation,

$$^0\boldsymbol{\omega} = \mathbf{R}\,{}^1\boldsymbol{\omega} \tag{4}$$

An efficient algorithm for the integration of (2) relies on the midpoint rule,

$$\mathbf{R}_{n+1} = \exp\!\left(\Delta t\,{}^0\mathbf{\Omega}_{n+\frac{1}{2}}\right)\mathbf{R}_n \tag{5}$$

with $\Delta t = t_{n+1} - t_n$ being the time step size. The update scheme (5) ensures that the orthogonality of the rotation matrix is conserved.[6] An obvious choice for the mid-point angular velocities is given by

$$^0\boldsymbol{\omega}_{n+\frac{1}{2}} = \frac{1}{2}\left({}^0\boldsymbol{\omega}_n + {}^0\boldsymbol{\omega}_{n+1}\right) = \frac{1}{2}\left(\mathbf{R}_n\,{}^1\boldsymbol{\omega}_n + \mathbf{R}_{n+1}\,{}^1\boldsymbol{\omega}_{n+1}\right) \tag{6}$$

where $^1\boldsymbol{\omega}_n$ and $^1\boldsymbol{\omega}_{n+1}$ are the measured, corotational angular velocity components at the n-th and $(n+1)$-th time step,

---

[6]The midpoint rule involves exactly one integration point and therefore leads to a multiplicative update of the rotation matrix, with both matrix factors being orthogonal and, thus, yielding an orthogonal matrix product. The rectangle rule has the same property but is less accurate, whereas the trapezoidal rule does *not* conserve the orthogonality, which leads to corrupt results. Higher-order integration schemes suffer from the same problem and are generally not justified for the integration of discrete data.
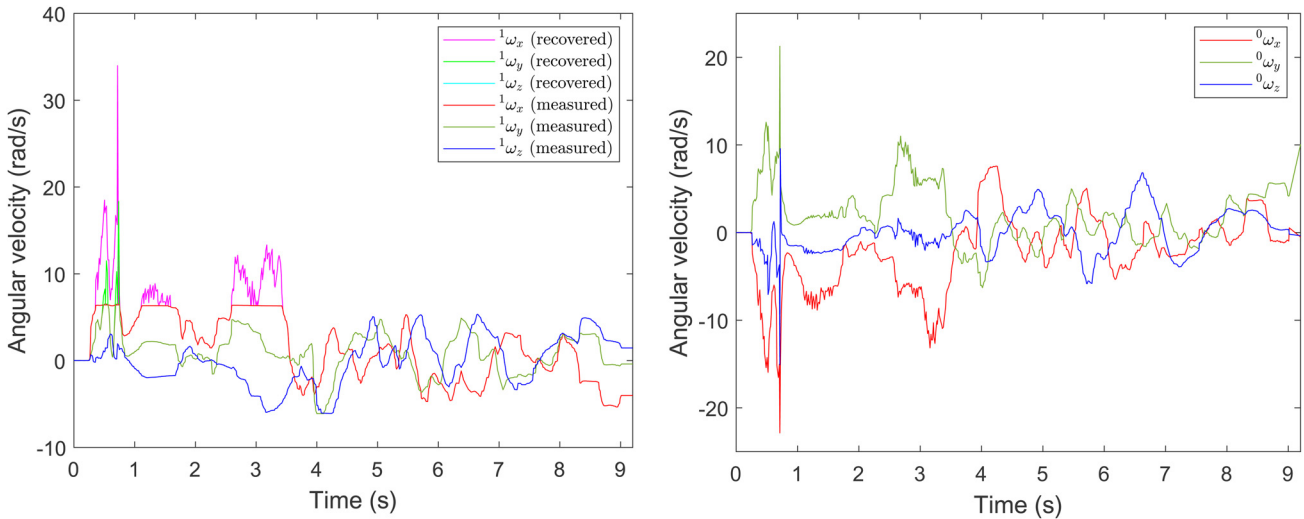
Figure 6. *Left:* Angular velocity components with respect to the corotating sensor coordinate system. Line colours red/dark green/blue refer to the measured values, magenta/green/cyan to the recovered ones. *Right:* Angular velocity components with respect to the global, inertial coordinate system.

respectively. Equation (6) delivers an implicit definition of components $^0\boldsymbol{\omega}_{n+1/2}$, which becomes apparent when inserting (5).

To derive additional advantage from the magnetometer data, the ansatz (6) is modified as follows. Use is made of the fact that the components of earth's magnetic field with respect to the global frame, $^0\mathbf{B}$, are virtually constant in time,

$$\mathbf{R}\,^1\mathbf{B} = {}^0\mathbf{B} = \text{const} \tag{7}$$

In particular, $\mathbf{R}_{n+1}\,^1\mathbf{B}_{n+1} = {}^0\mathbf{B}$. It is important to have in mind that $||^1\mathbf{B}|| = ||^0\mathbf{B}|| =: B_0$.

Inserting (5), a non-linear system of equations constraining the three components $^0\boldsymbol{\omega}_{n+1/2}$ is obtained,

$$\exp\left(\Delta t\,^0\boldsymbol{\Omega}_{n+\frac{1}{2}}\right)\mathbf{R}_n\,^1\mathbf{B}_{n+1} = {}^0\mathbf{B} \tag{8}$$

Note that the system (8) is under-determined. Together with the three equations (6), an over-determined system is obtained, from which the three components $^0\boldsymbol{\omega}_{n+1/2}^*$ can be determined via the least squares method,[7]

$$\mathbf{F}(\boldsymbol{\omega}^*) \equiv \begin{bmatrix} \Delta t\left\{\exp\left(\Delta t\,\boldsymbol{\Omega}^*\right)\mathbf{R}_n\,^1\boldsymbol{\omega}_{n+1} + {}^0\boldsymbol{\omega}_n - 2\,\boldsymbol{\omega}^*\right\} \\ \dfrac{w_{n+1}}{B_0}\left\{\exp\left(\Delta t\,\boldsymbol{\Omega}^*\right)\mathbf{R}_n\,^1\mathbf{B}_{n+1} - {}^0\mathbf{B}\right\} \end{bmatrix}$$
$$= \mathbf{0} \tag{9}$$

Both systems, (6) and (8), have been scaled, such that they are free of any physical unit. In addition, a factor w_n has been introduced, which allows to weight the two subsystems relatively to each other. This turns out to be beneficial, since the reliability of the measured magnetic field is not constant throughout the measurement period. The respective reliability can be estimated from the deviation of the norm $||^1\mathbf{B}_n||$ from its expected value B_0. On the basis of numerical experiments the following weighting function has been established,

$$w_n = \mathrm{e}^{-\left(p\frac{B_0 - ||^1\mathbf{B}_n||}{B_0}\right)^2}. \tag{10}$$

---

[7]In general, the evaluation of the matrix exponential function is computationally expensive. The exponential function of a skew-symmetric (3×3)-matrix, however, can be computed efficiently by means of the Rodrigues formula (Wittenburg, 2008, e.g.).

The parameter p is determined such that the noise of the obtained global magnetic field components is virtually the same for all three components $^0B_{x,y,z}(t)$, see Figure 10, yielding a value of $p = 5$. For each time step n, the system (9) can be solved for the $\boldsymbol{\omega}^*$ by means of the Gauss–Newton method (Björck, 1996). The rotation matrix is then updated via (5) with $^0\boldsymbol{\omega}_{n+\frac{1}{2}} = \boldsymbol{\omega}^*$.

With the help of the updated rotation matrix $\mathbf{R}_{n+1}$, the measured quantities $^1\mathbf{B}_{n+1}$ (magnetic field), $^1\boldsymbol{\omega}_{n+1}$ (angular velocity) and $^1\mathbf{a}_{n+1}$ (acceleration) are transformed to the global coordinate system via a passive rotation,

$$^0\{\mathbf{B},\boldsymbol{\omega},\mathbf{a}\}_{n+1} = \mathbf{R}_{n+1}\,^1\{\mathbf{B},\boldsymbol{\omega},\mathbf{a}\}_{n+1} \tag{11}$$

To specify the initial orientation of the sensor unit, the global coordinate system $(\mathbf{e}_x^0, \mathbf{e}_y^0, \mathbf{e}_z^0)$ is defined according to the geographic East-North-Up (ENU) convention: The global z and y axes are upward vertical and geographic north, respectively. At rest, the IMU measures an acceleration vector $^1\mathbf{a}_0 = -^1\mathbf{g}$, with $\mathbf{g}$ being earth's gravitational acceleration vector and a magnetic field $^1\mathbf{B}_0$, which is considered to originate solely from earth's magnetism. Correspondingly (Yun and others, 2008),

$$\mathbf{e}_x = \frac{^1\mathbf{B}_0 \times {}^1\mathbf{a}_0}{||^1\mathbf{B}_0 \times \mathbf{a}_0||}, \quad \mathbf{e}_y = \mathbf{e}_z \times \mathbf{e}_x, \quad \mathbf{e}_z = \frac{^1\mathbf{a}_0}{||\mathbf{a}_0||} \tag{12}$$

The vector components $^1\mathbf{a}_0$ and $^1\mathbf{B}_0$ have been determined by averaging the measured values over a time period of 0.2 s immediately before the sensor unit has been entrained by the avalanche. To be more precise, the declination D of earth's magnetic field has to be taken into account, such that

$$\mathbf{e}_x^0 = \cos D\,\mathbf{e}_x - \sin D\,\mathbf{e}_y, \quad \mathbf{e}_y^0 = \sin D\,\mathbf{e}_x + \cos D\,\mathbf{e}_y,$$
$$\mathbf{e}_z^0 = \mathbf{e}_z \tag{13}$$

A value of $D = 2.09705°$ has been extracted according to Schnegg (1998). Correspondingly, the initial orientation is given by the rotation matrix

$$\mathbf{R}_0 = \begin{bmatrix} \mathbf{e}_x^0 & \mathbf{e}_y^0 & \mathbf{e}_z^0 \end{bmatrix}^T \tag{14}$$

which is used to determine $^0\mathbf{B} = \mathbf{R}_0\,^1\mathbf{B}_0$ and to initialize the integration procedure.

4.1.2. Recovery of translational velocity and position

It is essential to distinguish between the 'kinematic' acceleration vector, here denoted as $^0\dot{\mathbf{v}}_n$, and the 'dynamic' acceleration vector $^1\mathbf{a}_n$, whose components are measured by the accelerometers. The former has to be understood as negative inertial force vector per mass, and the latter as guiding (or reaction) force per mass:[8] At rest, the kinematic acceleration is zero, $^0\dot{\mathbf{v}} = \mathbf{0}$, whereas an ideal accelerometer triad is expected to measure the reaction to Earth's acceleration, $^1\mathbf{a} = -^1\mathbf{g}$. In the course of an ideal ballistic motion, the kinematic acceleration equals Earth's acceleration, $^0\dot{\mathbf{v}} = {}^0\mathbf{g} = [\,0\;\;0\;\;-g\,]^T$, whereas inertial forces and earth's attraction cancel each other, such that $^1\mathbf{a} = \mathbf{0}$. Generally,

$$^0\dot{\mathbf{v}}_n = {}^0\mathbf{g} + \mathbf{R}_n\,{}^1\mathbf{a}_n \tag{15}$$

with

$$^0\mathbf{g} = -\mathbf{R}_0\,{}^1\mathbf{a}_0 = \begin{bmatrix} 0 & 0 & -\|{}^1\mathbf{a}_0\| \end{bmatrix}^T \tag{16}$$

For a hypothetically perfect calibration of the accelerometers, one expects $\|{}^1\mathbf{a}_0\|$ to match the local value of Earth's gravitational acceleration (Schwartz and Lindau, 2003).

Equation (15) delivers the kinematic acceleration of the reference point, to which the measured accelerations are referred (see Fig. 1). The origin of the sensor coordinate system is arbitrarily chosen to be located at the geometric centre of the (almost) spherical housing. The respective coordinates of the reference point are

$$^1\boldsymbol{\varepsilon} = \begin{bmatrix} 12 & -31 & -12 \end{bmatrix}^T \tag{17}$$

with an estimated accuracy of ±1 mm (Fig. 1). Taking this eccentricity into account, the kinematic acceleration vector of the centre point is obtained by compensating for the rotational inertia term, $\dot{\boldsymbol{\omega}} \times \boldsymbol{\varepsilon}$, and a centripetal acceleration, $\boldsymbol{\omega} \times (\boldsymbol{\omega} \times \boldsymbol{\varepsilon})$, see Wittenburg (2008),

$$
\begin{aligned}
^0\dot{\mathbf{v}}_{n+1}^{(C)} = {}&^0\mathbf{g} \\
&+ \mathbf{R}_{n+1}\big[{}^1\mathbf{a}_{n+1} - {}^1\dot{\boldsymbol{\omega}}_{n+1} \times {}^1\boldsymbol{\varepsilon} - {}^1\boldsymbol{\omega}_{n+1} \times ({}^1\boldsymbol{\omega}_{n+1} \times {}^1\boldsymbol{\varepsilon})\big]
\end{aligned}
\tag{18}
$$

The angular acceleration $\dot{\boldsymbol{\omega}}$ can be approximated by a symmetric finite difference,

$$^1\dot{\boldsymbol{\omega}}_{n+1} \approx \frac{^1\boldsymbol{\omega}_{n+2} - {}^1\boldsymbol{\omega}_n}{t_{n+2} - t_n} \tag{19}$$

An estimate of sensor unit velocities is obtained by integrating the kinematic accelerations (18) via the trapezoidal rule with $^0\mathbf{v}_0 = \mathbf{0}$,

$$^0\mathbf{v}_{n+1} = {}^0\mathbf{v}_n + \Delta t\,\frac{^0\dot{\mathbf{v}}_n + {}^0\dot{\mathbf{v}}_{n+1}}{2} \tag{20}$$

and, analogously, for the positions,

$$^0\mathbf{x}_{n+1} = {}^0\mathbf{x}_n + \Delta t\,\frac{^0\mathbf{v}_n + {}^0\mathbf{v}_{n+1}}{2} \tag{21}$$

To understand the role of eccentricity and to quantitatively assess its effect on velocity and position results, it is helpful to

imagine what the results of a hypothetically perfect tracking procedure (neither measurement nor integration errors) are expected to be: such procedure would deliver the trajectory of the centre point according to the translational motion superimposed by the spiralling path of the accelerometer reference point according to the rotational motion. Consequently, the trajectories of centre and reference point, respectively, would not deviate from each other by more than a distance of $\|{}^1\boldsymbol{\varepsilon}\|$. This gives rise to the assumption, that also under realistic circumstances, the influence of a small eccentricity on the trajectory is small, since the oscillating disturbances related to the extra terms in (18) will largely be suppressed by the smoothing effect of the numerical integration, as long as no parasitic aliasing occurs related to the specific sampling rate. This assumption must, of course, be verified on the basis of the experimental results, see the next section.

4.2. Quantitative analysis based on standard calibration

Initially, the numerical analysis of the recorded IMU data has been applied to the time span [0, 16] s, which covers the period of avalanche motion. Correspondingly, the explications of this section refer to this time span, having in mind that the results for $t > 9$ s are corrupt. To not present misleading results, most diagrams are restricted to the time span [0, 9.2] s. The onset of data failure at $t = 9.015$ s can thus be observed at the very end of the drawn curves. Wherever a larger time span is presented, this is explicitly indicated and unreliable features are clearly identified by a dashed line style.

All results presented in this section refer to a calibration of accelerometers and gyrometers performed via conventional calibration procedures relying on laboratory experiments. Such procedures are state-of-the-art. The corresponding details are therefore postponed to Appendix A. The calibration of magnetometers is also performed by means of a state-of-the-art algorithm. The present approach, however, deviates from the standard procedure in one important aspect: to optimally account for the local conditions of Earth's magnetic field, the algorithm is supplied with magnetometer data recorded in the course of the avalanche experiment, i.e. with in situ data, rather than with laboratory data. Details can be found in Appendix A.

4.2.1. Slope coordinate system

It is a favourable circumstance that the relevant section of the terrain which covers the first 9 s of the sensor unit motion is virtually planar and can thus be approximated by an inclined plane with an inclination of $\alpha \approx 32°$. The projection of the vertical axis $\mathbf{e}_z^0$ onto this plane will be called the *slope secant*. The name derives from the fact that it is determined from the TLS terrain model and passes through the starting point of the sensor unit and a corresponding point at the terrain surface in a distance of 120 m, which is approximately the travelling distance after 9 s. The (exactly straight) slope secant approximates the (almost straight) slop line, which is the projection of the vertical axis onto the actual terrain surface. Correspondingly, an additional Cartesian coordinate frame $(\mathbf{e}_x^s, \mathbf{e}_y^s, \mathbf{e}_z^s)$, which is particularly useful for the interpretation of the tracking results, can be defined in a straight-forward manner: the first basis vector $\mathbf{e}_x^s$ is aligned with the slope secant. The second basis vector $\mathbf{e}_y^s = \mathbf{e}_z^0 \times \mathbf{e}_x^s$ is horizontal and tangent to the corresponding contour line. The third one, $\mathbf{e}_z^s = \mathbf{e}_x^s \times \mathbf{e}_y^s$ represents the direction normal to the terrain.[9] The so defined basis will be called the *slope coordinate system* (or *frame*) and its axis directions are referred to as *longitudinal* $(\mathbf{e}_x^s)$, *lateral* $(\mathbf{e}_y^s)$ and *transverse* $(\mathbf{e}_z^s)$. The rotation tensor

---

[8] Considering Newton's law of motion in the sense of d'Alembert: $\mathbf{F}_i + \mathbf{F}_a + \mathbf{F}_r = \mathbf{0}$, with $\mathbf{F}_i = -m\dot{\mathbf{v}}$ being the inertial force (vector), $\mathbf{F}_a$ the applied force and $\mathbf{F}_r$ the guiding or reaction force.

[9] Planarity is, however, *not* essential. A corresponding slope coordinate system can be defined on any smooth surface with a smooth gradient field.

transforming the inertial frame ($\mathbf{e}_x^0$, $\mathbf{e}_y^0$, $\mathbf{e}_z^0$) into the slope frame is given by

$$\mathbf{Q}_s = \begin{bmatrix} \mathbf{e}_x^s & \mathbf{e}_y^s & \mathbf{e}_z^s \end{bmatrix}. \tag{22}$$

4.2.2. Rotational motion

The measurement range of the gyrometers, which has been chosen too small, has lead to a cut-off of a few angular velocity peaks somewhat above $\pm 6\,\mathrm{rad\,s}^{-1}$ (which is, in fact, larger than the nominal range of $\pm 300°\,\mathrm{s}^{-1}$). Luckily, whenever this has happened, not more than one out of the three angular velocity components has been affected by saturation. Therefore, the missing component can be recovered with the help of the magnetometer data. The corresponding procedure is described in detail in Appendix B. The results are shown in Figure 6 (left). The recovered curves provide a smooth continuation of the measured ones.

An estimate $\mathbf{R}_n$ for the angular orientation of the sensor unit at any time step t_n in the considered time interval is obtained by integrating the calibrated gyrometer data (Eqn (5)). For this purpose, the mid-point values of angular velocity components, $^0\boldsymbol{\omega}_{n+1/2}$, are calculated by solving the overdetermined, non-linear equation system (9) via the Gauß–Newton method. The integration procedure is initialized with the starting orientation given by (14). It shall be mentioned here (and will be discussed subsequently), that the recovered angular orientation relies not only on angular rates, but also on magnetometer data and on accelerometer data (via the initial orientation). The rotational motion so obtained can be visualized and interpreted favourably via the evolution of the rotation (or *Euler*) vector $\boldsymbol{\varphi}_n$, which is implicitly defined by

$$\mathbf{R}_n \mathbf{R}_0^T = \exp \boldsymbol{\Phi}_n \tag{23}$$

Wittenburg (2008) with $\boldsymbol{\Phi}_n$ being the skew-symmetric matrix composed from the components of vector $\boldsymbol{\varphi}_n$, compare Eqn (3). The matrix $\mathbf{R}_n \mathbf{R}_0^T$ refers to the orientation at time step t_n relatively to the initial orientation $\mathbf{R}_0$. It shall be noticed that the components $\mathbf{R}_n$ and $\boldsymbol{\varphi}_n$ refer to the global, inertial coordinate system ($\mathbf{e}_x^0$, $\mathbf{e}_y^0$, $\mathbf{e}_z^0$) as well as to the local, moving coordinate system ($\mathbf{e}_x^1$, $\mathbf{e}_y^1$, $\mathbf{e}_z^1$) at the same time, i.e. $^0\mathbf{R}_n = {}^1\mathbf{R}_n$ and $^0\boldsymbol{\varphi}_n = {}^1\boldsymbol{\varphi}_n$ (Wittenburg, 2008).[10] For a straight-forward interpretation of the rotational motion it is, however, beneficial to express the rotation vector with respect to the slope frame ($\mathbf{e}_x^s$, $\mathbf{e}_y^s$, $\mathbf{e}_z^s$), indicated through the left superscript symbol 's',

$$^s\boldsymbol{\varphi}_n = \mathbf{Q}_s^T \boldsymbol{\varphi}_n \tag{24}$$

The result is drawn in Figure 7 and compared to the angular velocity components $^s\boldsymbol{\omega}_n = \mathbf{Q}_s^{T0}\boldsymbol{\omega}_n$ with respect to the same frame. It can be concluded from these diagrams that in the course of the first 3.2 s the rotational motion is dominated by a fast rotation about the horizontal $\mathbf{e}_y^s$-axis at an average speed of $7.81\,\mathrm{rad\,s}^{-1} \approx 477°\,\mathrm{s}^{-1} \approx 1.24$ rounds per second. In this time period, the sensor unit performs a number of four full twits about the $\mathbf{e}_y^s$-axis. The first twist is the fastest one with an average speed of $12.36\,\mathrm{rad\,s}^{-1} \approx 708°\,\mathrm{s}^{-1} \approx 1.97$ rounds per second and an instantaneous velocity peak of approximately $35\,\mathrm{rad\,s}^{-1} \approx 2000°\,\mathrm{s}^{-1} \approx 5.5$ rounds per second.[11] For $t > 3.2$ s, the rotational motion continues at a lower speed and without a stable rotation axis. As mentioned before, the results for $t > 9$ s are

---

[10]This is the reason why the left superscript index specifying the reference basis has been skipped for $\mathbf{R}_n$ and $\boldsymbol{\varphi}_n$.

[11]The latter value might serve as a reference for the configuration of future measurement set-ups.

corrupt due to a data gap and are, thus, not displayed here. A demonstrative visualization of the rotational motion is presented in Figure 8. For the visualization, the path $\mathbf{r}(t)$ drawn there is the trajectory of a point on a hypothetical sphere with an (arbitrarily chosen) radius of $r = 5$ m which is thought to move and rotate in the same way as the sensor unit does, i.e.

$$\mathbf{r}(t_n) = \mathbf{x}_n + \mathbf{R}_n\big(r\mathbf{e}_z^0\big)$$

4.2.3. Magnetic field

It has been described in detail how the magnetometer data can be used to stabilize the integration of angular rates (Section 4.1.1) and to bridge short gaps with deficient gyrometer data (Appendix B). In addition, the measured magnetic flux density can give an evidence to assess the reliability of the recovered angular orientations. In this context, a proper calibration is crucial. At the absence of ferromagnetic disturbances it can be assumed that the vector of the magnetic flux density, and thus its components with respect to the inertial frame, $^0\mathbf{B}$, are virtually constant in space and time. Consequently, the norm of the local components $\|{}^1\mathbf{B}\|$ is expected to be constant as well,

$$\|{}^1\mathbf{B}(t)\| = \|{}^0\mathbf{B}(t)\| = \mathrm{const} \tag{25}$$

A sufficiently accurate fulfilment of Eqn (25) is thus a necessary condition for the measured values and, in particular, for the calibration to be reliable. A significant deviation from the expected value is used to define a quantitative reliability measure according to Eqn (10), which governs the effect of the magnetometer data on the angular orientations, compare Figure 9.

A necessary condition for the reliability of the recovered orientations $\mathbf{R}(t)$ is given by the constancy of the global components of $\mathbf{B}$,

$$^0\mathbf{B} = \mathbf{R}(t)^1\mathbf{B}(t) = \mathrm{const} \tag{26}$$

which is illustrated in Figure 10. It is also worth to discuss the direction of vector $\mathbf{B}$ specified via spherical (azimuthal and polar) angles, φ and ϑ. Defining these angles with respect to the global ENU coordinate system ($\mathbf{e}_x^0$, $\mathbf{e}_y^0$, $\mathbf{e}_z^0$), one has

$$\varphi = \arctan\frac{^0B_y}{^0B_x} = 90° - D, \quad \vartheta = \arccos\frac{^0B_z}{\|\mathbf{B}\|} = 90° + I \tag{27}$$

with declination D and inclination I.

According to Schnegg (1998), at the time and location of the experiment, the corresponding values are $D_0 = 2.09705°$ and $I_0 = 62.81433°$. The declination has already been used for the specification of the starting orientation in (13) and can therefore *not* serve for any further verification. The inclination, on the other hand, has not been considered so far. Calculating the latter from the global magnetic field components via Eqn (27b), values are obtained which oscillate around a mean value of $\bar{I} \approx 61.19°$ with a standard deviation of $1.3°$ (see Fig. 10). Thus, a deviation of $I_0 - \bar{I} \approx 1.62°$ from the expected value I_0 is observed. This result reveals a moderate error in the recovered orientations.

4.2.4. Translational motion

In Figure 11, at the left-hand side, the dynamic acceleration components with respect to the sensor frame, $^1\mathbf{a}$, are drawn. These are the values measured by the accelerometers and subjected to laboratory calibration. At the right-hand side, the kinematic acceleration components with respect to the inertial frame, $^0\dot{\mathbf{v}}$, Eqn (18), are plotted. It is emphasized that, in contrast to the $^1\mathbf{a}$, the
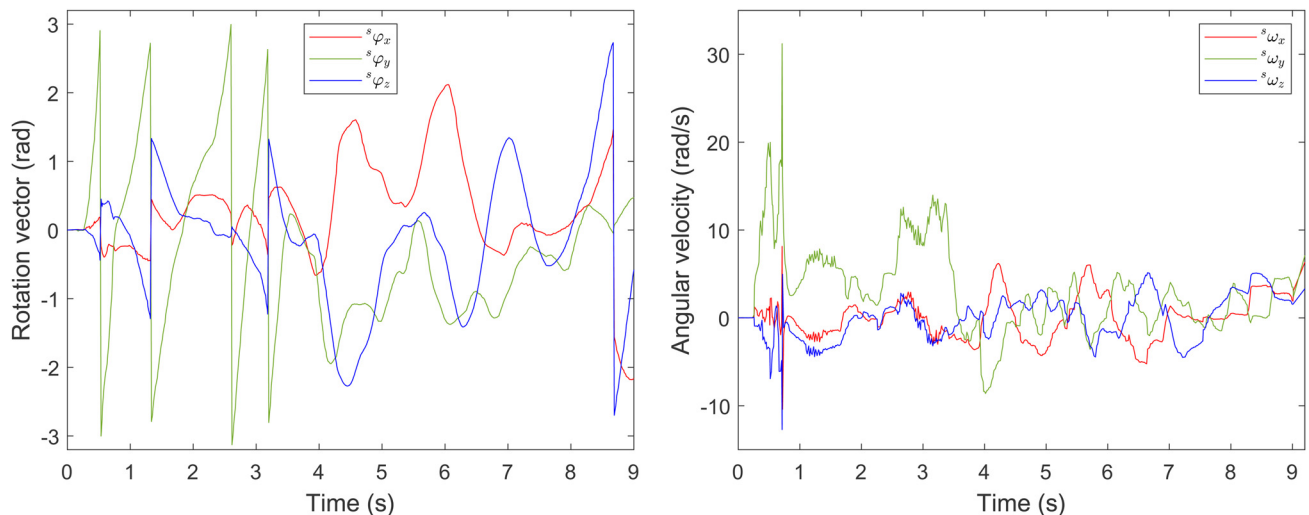
Figure 7. Rotation vector (left) and angular velocity (right) components with respect to the slope frame.
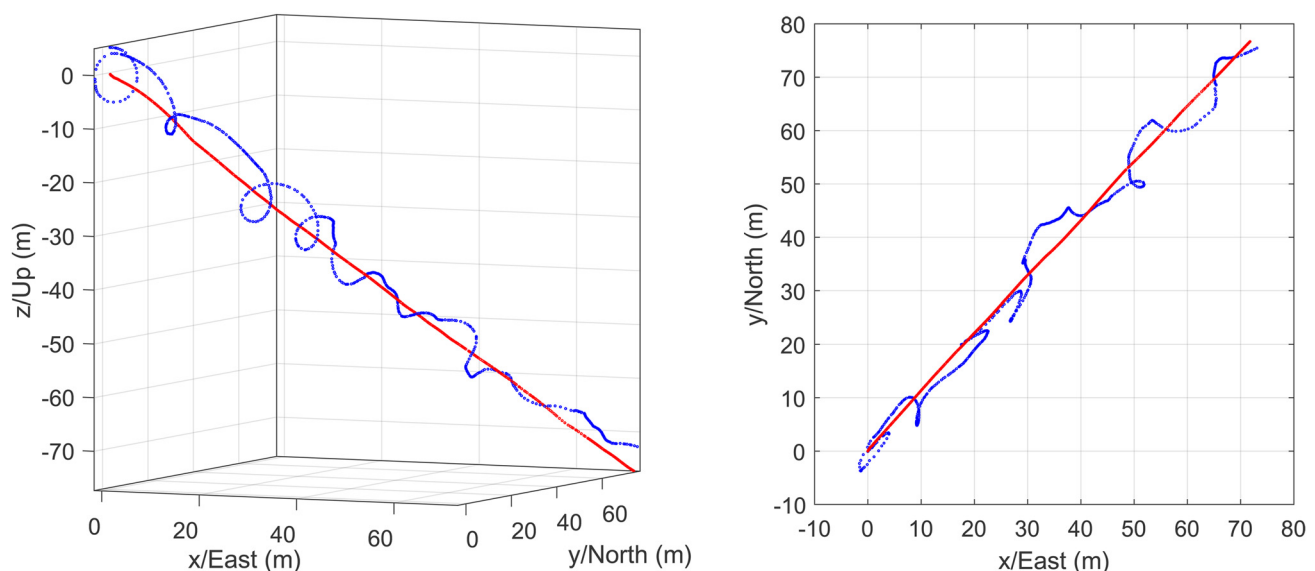

Figure 8. *Red:* Trajectory of the centre of the sensor housing, $\mathbf{x}(t)$, corresponding to the time interval [0, 9] s. *Blue:* Trajectory of a hypothetical tracing point in a constant distance of 5 m from the centre, $\mathbf{r}(t)$, for visualization of the rotational motion. *Left:* Axonometric view. *Right:* Top view, i.e. a normal projection of the trajectory onto a horizontal plane.

$^0\dot{\mathbf{v}}$ rely on the whole set of measurement data, since the rotation matrix $\mathbf{R}$ is required for the coordinate transformation (11).

The clear representation of ballistic motion is considered as a certain evidence for the reliability of the measurements: a pronounced ballistic phase starts at $t \approx 0.85$ s and is followed by several shorter ones, especially in the time period from $t \approx 7.6$ s to $t \approx 9$ s, during which a sort of saltational motion occurs (short ballistic phases interrupted by impacts; see Fig. 12). The ballistic phases are represented by the expected values of $^0\dot{\mathbf{v}} = [0 \ 0 \ -g]^T$.

Knowing the evolution of the kinematic acceleration, the sensor unit trajectory can be recovered according to Section 4.1.2. Projections of the obtained trajectory and of the reference tube (Section 2) are depicted in Figure 13. The plots refer to the whole time span [0, 16] s in order to demonstrate the parasitic effect of the data gap at $t \approx 9$ s. Correspondingly, the second third of the path (dashed lines) might be dismissed. Note that the reference domain applying to the top view (left diagram) is also drawn in Figure 2 and recall that the reference domain for the vertical section (right diagram) is aligned with the terrain surface (including the snow cover) and has an assumed vertical span of ±1 m.

Figure 13 also demonstrates the influence of the eccentricity $^1\boldsymbol{\varepsilon}$ included in Eqn (18): the blue and red curves refer to an evaluation of (18) with and without consideration of eccentricity, i.e. with $^1\boldsymbol{\varepsilon}$ given by (17) and with $^1\boldsymbol{\varepsilon} = \mathbf{0}$, respectively. The small extend of the deviation of the corresponding results indicates that the considerations of Section 4.1.2 concerning the effect of eccentricity are applicable. In particular, the sensitivity of the tracking results to a small change of the eccentricity vector is negligible. Accordingly, an eccentricity given by (17) is considered for all subsequent computations.

A comparison of the recovered trajectory with the reference reveals a somewhat unexpected behaviour: referring to the top view in Figure 13 (left), the numerical result matches the reference surprisingly well. A slight but progressive lateral movement is observed. The most likely explanation for this behaviour is a (quadratic) numerical drift, which is expected due to the twofold integration procedure leading to the position results. However, it cannot be excluded, that (to a small extent) the lateral movement also reflects a physical motion. In contrast, the vertical section in Figure 13 (right) reveals a significant deviation from the terrain
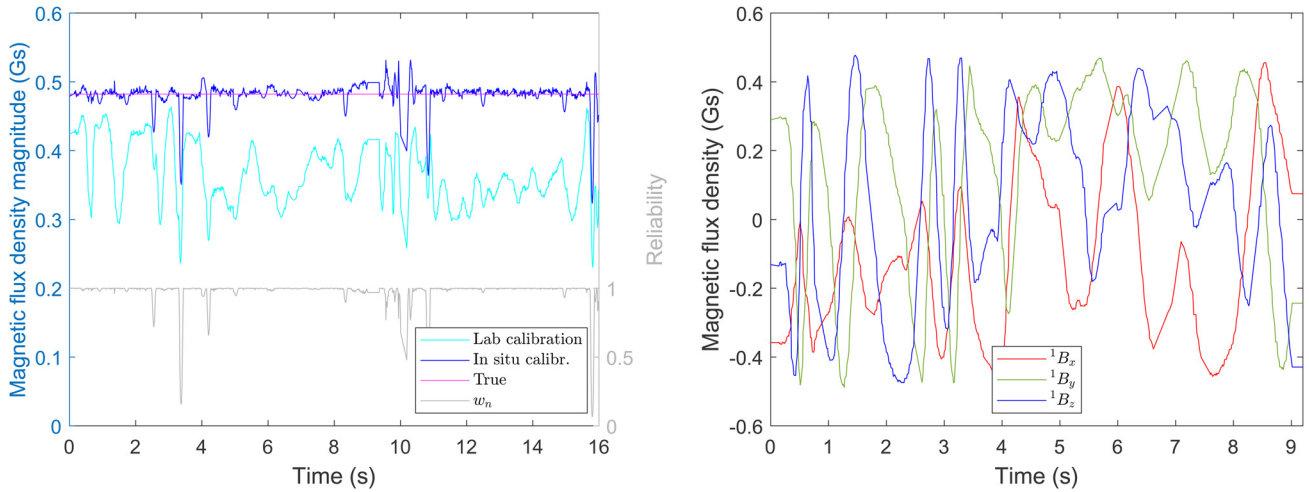
Figure 9. *Left*: Vector norm of the local components of the magnetic flux density, $\|{}^1\mathbf{B}\|$, subjected to a calibration under laboratory conditions carried out some time after the avalanche experiment (cyan) and to an in situ calibration according to Appendix B (blue). The reliability measure (gray) is calculated from (10). *Right*: Local components of the magnetic flux density, ${}^1\mathbf{B}_k$, subjected to in situ calibration.
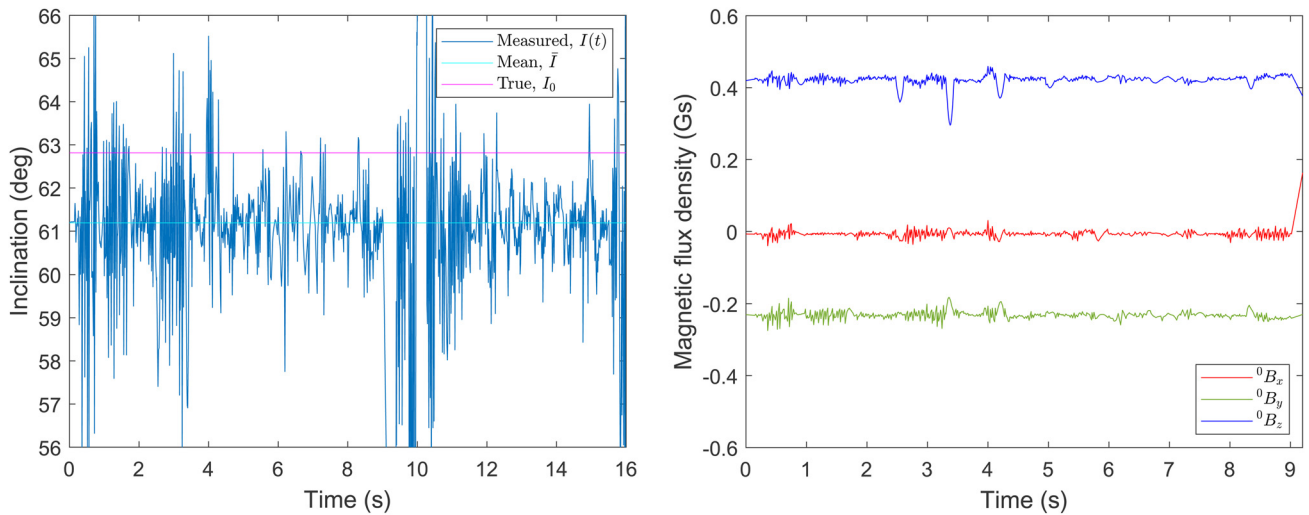

Figure 10. *Left*: Inclination $I(t_n)$ calculated from ${}^0\mathbf{B}(t_n)$ via Eqn (27b), its mean value $\bar{I}$ and the true value I_0. *Right*: Global components of the magnetic flux density, ${}^0B_{x,y,z}$. The B components involved are subjected to in situ calibration, whereas the initial orientation relies on accelerometer data subjected to laboratory calibration.
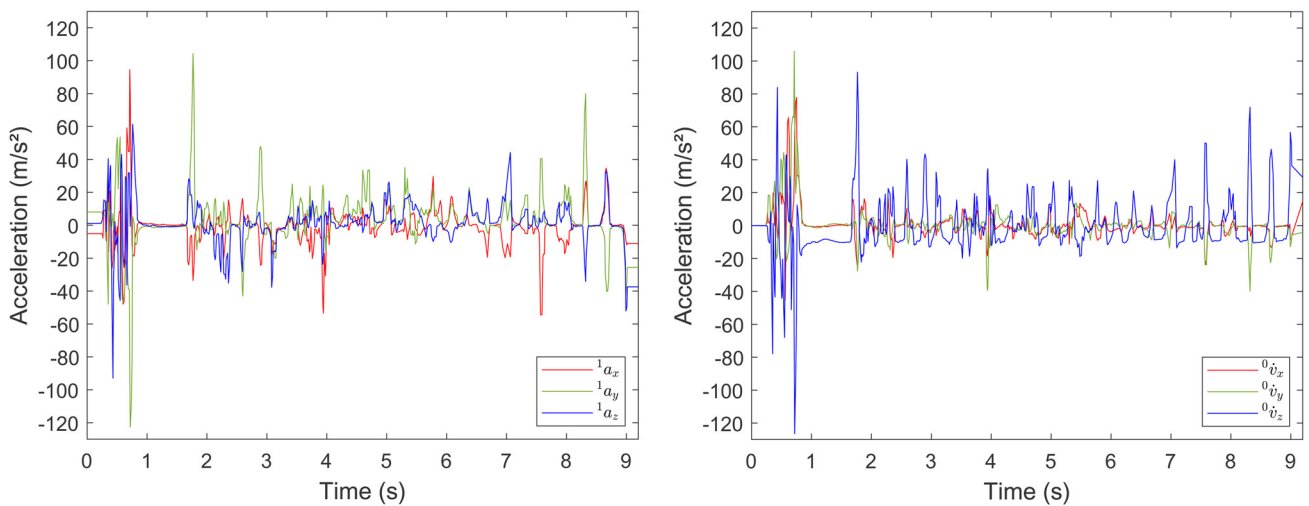

Figure 11. *Left*: Dynamic acceleration components with respect to the local coordinate system. *Right*: Kinematic acceleration components with respect to the global coordinate system.
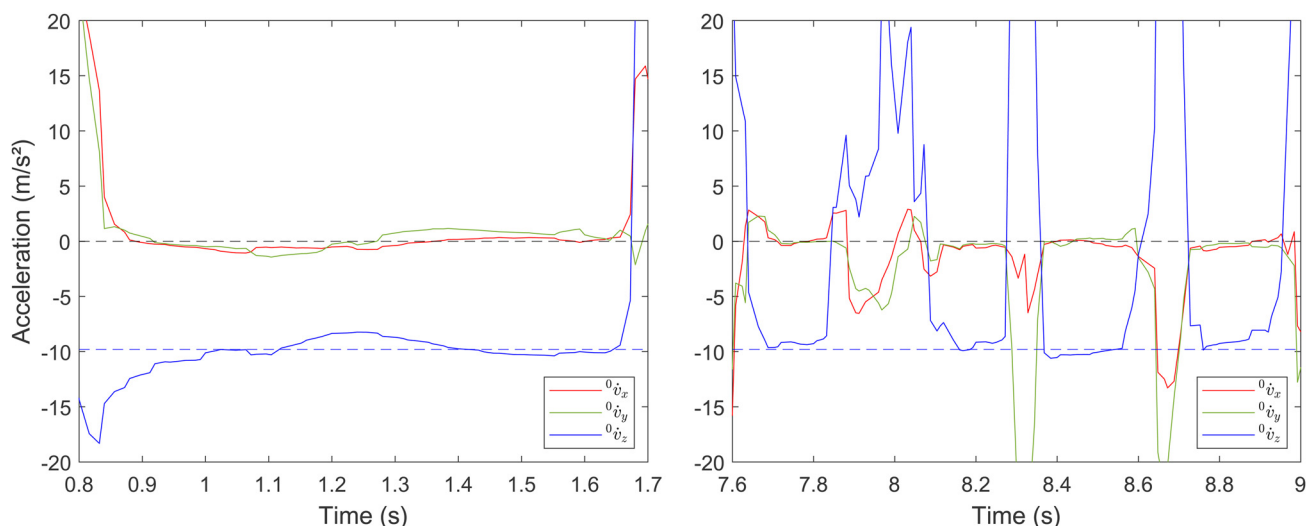
Figure 12. Kinematic acceleration components related to the global frame: selected time intervals dominated by ballistic or saltational motion.
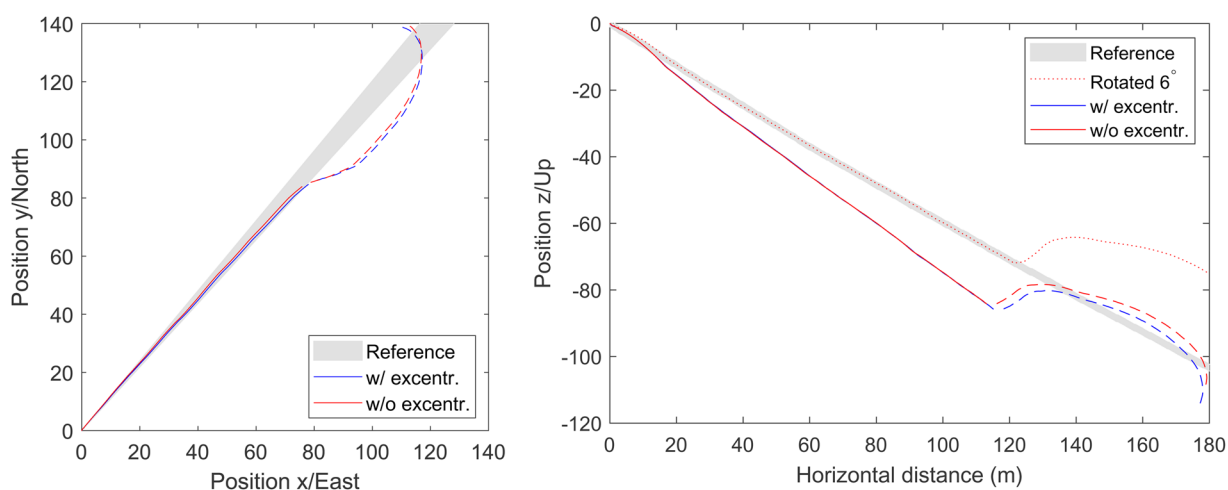

Figure 13. Sensor unit trajectory recovered from IMU data according to Section 4.1.2 and compared to the reference defined in Section 1. The heavy deviations from the reference in the second third of the path (dashed lines) are a result of the data gap at $t \approx 9$ s and might be dismissed. *Left:* Top view, i.e. a normal projection onto a horizontal plane. The blue and red curves refer to an evaluation of (18) with and without consideration of eccentricity, respectively. *Right:* Vertical section, i.e. a normal projection onto a vertical plane passing through the slope line.

surface, which is physically impossible. This deviation is more like an overall misalignment rather than an expected drift, since it is present even at the beginning of the movement and is virtually constant throughout the path (until the data gap occurs at $t \approx 9$ s). This observation is supported by the dotted red line in the right diagram, which results from a rotation of the solid red line by an assumed angle of $6°$ in the vertical section plane.

5. Accelerometer in situ calibration

5.1. Theory

In this section, a theory is presented, which provides an explanation for the misalignment of the recovered trajectory, addressed at the end of the previous section. In addition, the underlying assumption leads to a novel procedure to eliminate the misalignment error, for which the term 'in situ calibration' is suggested.

If the misalignment would originate from stochastic errors, its magnitude should be small at the beginning and should increase more or less monotonically afterwards, which is not the case. Consequently, it can be concluded that the source of error is of systematic nature. At a first glance, a wrong initial orientation

$\mathbf{R}_0$ would deliver an obvious explanation for the misalignment. This possibility, however, can be excluded by the verification of the orientation results presented in Section 4.2.3. Instead, it is postulated that the observed deviation originates from an inaccurate calibration of accelerometers. This assumption appears realistic, since the original calibration procedure (Appendix A) has been carried out under laboratory conditions 5 years after the avalanche experiment. Subsequently, it will be explicated, how a recalibration can be obtained on the basis of the data recorded in the course of the avalanche event, i.e. on the basis of in situ data. Recall that a related approach for the recalibration of magnetometers has been addressed in Section 4.2.3. Although these two fields of application (accelerometers and magnetometers) require two fundamentally different procedures, they have one important aspect in common: the reliability of the recalibration procedures essentially relies on the characteristics of the rotational motion. To start with, this shall be demonstrated for the case of magnetometer recalibration: mathematically speaking, the subset of orientations $\mathbf{R}_n$ occurring in the course of the motion must be evenly distributed in the set of all possible orientations; or, less abstract, the tips of normalized vectors $^1\mathbf{B}_n/\|^1\mathbf{B}_n\|$ must be evenly distributed on the unit sphere. The more bias occurs

among this distribution (i.e. the less complex the rotational motion is), the worse is the conditioning of the equation system determining the calibration parameters and thus, the lower is the reliability of its solution (Appendix A). Although less obvious, an analogous statement holds for the accelerometer recalibration. In the present case, the orientations are spread over the whole sphere but are far from being uniformly distributed (Fig. 21). It turns out, however, that such a degree of uniformity is sufficient to achieve valuable results.

5.1.1. Accelerometer error model

The recalibration of the three-axis accelerometer based on in situ data relies on a common, linear error model, similar to the one which has already been used for the standard calibration procedure (Appendix A): it is assumed that the 'true' acceleration values $^1\mathbf{a}_n$ are related to the measured ones, $^1\tilde{\mathbf{a}}_n$, via

$$^1\mathbf{a}_n = (\mathbf{I} + \mathbf{C})^1\tilde{\mathbf{a}}_n + g\mathbf{b}_0 + g\tau_n\mathbf{b}_1 \tag{28}$$

Here, the calibration matrix $\mathbf{A} = \mathbf{I} + \mathbf{C}$ is assumed to deviate only slightly from the identity matrix $\mathbf{I}$. It allows for scaling errors, non-orthogonality and misalignment of the physical sensor axes relatively to the axes of the sensor coordinate system. The additive offset consists of a constant part (bias) $g\mathbf{b}_0$ and a linear drift $g\mathbf{b}_1$. Earth's acceleration g has been premultiplied to achieve calibration parameters which are independent of the choice of physical units. Due to the same reason, a dimensionless time parameter is used,

$$\tau_n = \frac{t_n - t_0}{t_N - t_0} \in [0, 1] \tag{29}$$

with N being the index of the last considered time step. The recalibration also affects $^0\mathbf{g}$ (Eqn (16)), which becomes

$$^0\mathbf{g} = -\mathbf{R}_0{}^1\mathbf{a}_0 = \begin{bmatrix} 0 & 0 & -\left\|(\mathbf{I} + \mathbf{C})^1\tilde{\mathbf{a}}_0 + g\mathbf{b}_0\right\| \end{bmatrix}^T \tag{30}$$

For the proposed implementation, the 'true' values are adopted, i.e. $^0\mathbf{g} = \begin{bmatrix} 0 & 0 & -g \end{bmatrix}^T$ with $g = 9.802$ m/s^{-2} for the local region.[12] The kinematic acceleration vectors (Eqn (15)) now read

$$^0\dot{\mathbf{v}}_n = {}^0\mathbf{g} + \mathbf{R}_n\big[(\mathbf{I} + \mathbf{C})^1\tilde{\mathbf{a}}_n - g\mathbf{b}_0 - g\tau_n\mathbf{b}_1\big] \tag{31}$$

By rearranging the calibration parameters

$$\mathbf{C} = \begin{bmatrix} c_1 & c_4 & c_7 \\ c_2 & c_5 & c_8 \\ c_3 & c_6 & c_9 \end{bmatrix}, \quad \mathbf{b}_0 = \begin{bmatrix} b_1 \\ b_2 \\ b_3 \end{bmatrix}, \quad \mathbf{b}_1 = \begin{bmatrix} b_4 \\ b_5 \\ b_6 \end{bmatrix} \tag{32}$$

the vectors

$$\mathbf{c} = \begin{bmatrix} c_1 \dots c_9 \end{bmatrix}^T, \quad \mathbf{b} = \begin{bmatrix} b_1 \dots b_6 \end{bmatrix}^T \tag{33}$$

are obtained, by which means Eqn (31) can be given a concise shape,

$$^0\dot{\mathbf{v}}_n = {}^0\tilde{\dot{\mathbf{v}}}_n + \mathbf{A}_n''\mathbf{b} + \mathbf{B}_n''\mathbf{c} \tag{34}$$

Therein,

$$^0\tilde{\dot{\mathbf{v}}}_n = {}^0\mathbf{g} + \mathbf{R}_n{}^1\tilde{\mathbf{a}}_n \tag{35}$$

are the kinematic acceleration vectors ahead of recalibration. The (3×6)-matrices

$$\mathbf{A}_n'' = g\begin{bmatrix} \mathbf{R}_n & \tau_n\mathbf{R}_n \end{bmatrix} \tag{36}$$

impart the correction according to bias and drift, whereas the (3×9)-matrices

$$\mathbf{B}_n'' = \begin{bmatrix} \mathbf{b}_{11}^{(n)} & \mathbf{b}_{21}^{(n)} & \mathbf{b}_{31}^{(n)} & \mathbf{b}_{12}^{(n)} & \mathbf{b}_{22}^{(n)} & \mathbf{b}_{32}^{(n)} & \mathbf{b}_{13}^{(n)} & \mathbf{b}_{23}^{(n)} & \mathbf{b}_{33}^{(n)} \end{bmatrix} \tag{37}$$

are related to the correction of scaling, non-orthogonality and misalignment. They are composed of columns

$$\mathbf{b}_{ij}^{(n)} = \mathbf{R}_{:,i}^{(n)}\,{}^1\tilde{a}_j^{(n)} \tag{38}$$

where $\mathbf{R}_{:,i}^{(n)}$ denotes the i-th column of the rotation matrix $\mathbf{R}_n$ and $^1\tilde{a}_j^{(n)}$ the j-th component of vector $^1\tilde{\mathbf{a}}_n$.

The improved kinematic accelerations (34) yield improved velocity and position vectors,

$$^0\mathbf{v}_n = \int_{t_0}^{t_n} {}^0\dot{\mathbf{v}}(t)\,\mathrm{d}t = {}^0\tilde{\mathbf{v}}_n + \mathbf{A}_n'\mathbf{b} + \mathbf{B}_n'\mathbf{c} \tag{39}$$

$$^0\mathbf{x}_n - {}^0\mathbf{x}_0 = \int_{t_0}^{t_n} {}^0\mathbf{v}(t)\,\mathrm{d}t = {}^0\tilde{\mathbf{x}}_n + \mathbf{A}_n\mathbf{b} + \mathbf{B}_n\mathbf{c} - {}^0\mathbf{x}_0 \tag{40}$$

Again, $^0\tilde{\mathbf{v}}_n$ and $^0\tilde{\mathbf{x}}_n$ denote the results ahead of recalibration, and

$$\mathbf{A}_n' = \int_{t_0}^{t_n} \mathbf{A}''(t)\,\mathrm{d}t, \quad \mathbf{B}_n' = \int_{t_0}^{t_n} \mathbf{B}''(t)\,\mathrm{d}t \tag{41}$$

$$\mathbf{A}_n = \int_{t_0}^{t_n} \mathbf{A}'(t)\,\mathrm{d}t, \quad \mathbf{B}_n = \int_{t_0}^{t_n} \mathbf{B}'(t)\,\mathrm{d}t \tag{42}$$

The integration is again performed via the trapezoidal rule. Correspondingly, the integral operations in Eqns (39)–(42) have to be understood as

$$\int_{t_0}^{t_n} f(t)\,\mathrm{d}t := \sum_{m=1}^{n} \frac{1}{2}\left(f_{m-1} + f_m\right)\left(t_m - t_{m-1}\right) \tag{43}$$

5.1.2. Topography constraint

In fact, the sensor unit has moved close to the topographic surface (terrain). Consequently, the recovered trajectory is also supposed to develop close to this surface. This gives rise to postulate a *soft* constraint either at the *velocity level*,

$$\sum_{n=1}^{N} \left(\mathbf{k}^T\mathbf{v}_n\right)^2 \quad \rightarrow \quad \text{Min!} \tag{44}$$

or at the *position level*,

$$\sum_{n=1}^{N} \left[\mathbf{k}^T(\mathbf{x}_n - \mathbf{x}_0)\right]^2 \quad \rightarrow \quad \text{Min!} \tag{45}$$

with $\mathbf{k}$ being the vector normal to the topographic surface. Equations (44) and (45) claim that the component normal to the terrain either of the velocity or of the relative position is

minimum in a least squares sense. To formulate these constraint conditions, the surface normal vector $\mathbf{k}$ is required, which can, in principle, be obtained from the TLS data. In the present case, $\mathbf{k}$ is almost constant and can be approximated by $\mathbf{k} = \mathbf{e}_z^s$ (Section 4.2.1). This circumstance makes the implementation significantly easier. It is, however, *not* a mandatory requirement for the method to work properly. Inserting (39) and (40), the constraint conditions (44) and (45) become

$$\left\| \tilde{\mathbf{v}}_\perp + \mathbf{A}'_\perp \mathbf{b} + \mathbf{B}'_\perp \mathbf{c} \right\|^2 \quad \rightarrow \quad \text{Min!} \tag{46}$$

$$\left\| \tilde{\mathbf{x}}_\perp + \mathbf{A}_\perp \mathbf{b} + \mathbf{B}_\perp \mathbf{c} \right\|^2 \quad \rightarrow \quad \text{Min!} \tag{47}$$

Conditions (46) and (47) are equivalent to the overdetermined systems of equations,

$$\begin{bmatrix} \mathbf{A}' & \mathbf{B}'_\perp \end{bmatrix} \begin{bmatrix} \mathbf{b} \\ \mathbf{c} \end{bmatrix} = -\tilde{\mathbf{v}}_\perp, \quad \begin{bmatrix} \mathbf{A}_\perp & \mathbf{B}_\perp \end{bmatrix} \begin{bmatrix} \mathbf{b} \\ \mathbf{c} \end{bmatrix} = -\tilde{\mathbf{x}}_\perp \tag{48}$$

respectively. For conciseness, the following $(N \times 1)$-vectors,

$$\tilde{\mathbf{v}}_\perp = \begin{bmatrix} \mathbf{k}^T \tilde{\mathbf{v}}_1 & \dots & \mathbf{k}^T \tilde{\mathbf{v}}_N \end{bmatrix}^T \tag{49}$$

$$\tilde{\mathbf{x}}_\perp = \begin{bmatrix} \mathbf{k}^T (\tilde{\mathbf{x}}_1 - \mathbf{x}_0) & \dots & \mathbf{k}^T (\tilde{\mathbf{x}}_1 - \mathbf{x}_0) \end{bmatrix}^T \tag{50}$$

as well as $(N \times 6)$- and $(N \times 9)$-matrices,

$$\mathbf{A}_\perp^{(\prime)} = \begin{bmatrix} \mathbf{k}^T \mathbf{A}_1^{(\prime)} \\ \vdots \\ \mathbf{k}^T \mathbf{A}_N^{(\prime)} \end{bmatrix}, \quad \mathbf{B}_\perp^{(\prime)} = \begin{bmatrix} \mathbf{k}^T \mathbf{B}_1^{(\prime)} \\ \vdots \\ \mathbf{k}^T \mathbf{B}_N^{(\prime)} \end{bmatrix} \tag{51}$$

have been introduced. Each of Eqns (48a) and (48b) constitutes an overdetermined, linear system of N equations for the $6 + 9 = 15$ unknowns contained in vectors $\mathbf{b}$ and $\mathbf{c}$. As discussed at the beginning of Section 5, the rotational motion involved must display a certain degree of complexity, to ensure that matrices (51a) and (51b) have full rank (i.e. 6 and 9, respectively). Consequently, each of the two equation systems yields a unique solution, which will be denoted $(\mathbf{b}_x, \mathbf{c}_x)$ for the position level constraint and $(\mathbf{b}_v, \mathbf{c}_v)$ for the velocity level.

5.1.3. Regularization
Determining the calibration parameters is a sort of inverse problem. In fact, none of the solutions of systems (48) is feasible, since at least some of the calibration parameters obtained (their absolute values) are too large, i.e. in the order of 1. This contrasts the original intention to search for a *small* correction of pre-calibrated values. Accordingly, the minimization problem has to be reformulated to search for a compromise between minimizing the overall deviation from the topographic surface and minimizing the calibration parameters. To this end, the objective functions are enriched by regularization terms,

$$f_v(\mathbf{b}, \mathbf{c}) := \left\| \tilde{\mathbf{v}}_\perp + \mathbf{A}'_\perp \mathbf{b} + \mathbf{B}'_\perp \mathbf{c} \right\|^2 + \rho g T \left(\|\mathbf{b}\|^2 + \|\mathbf{c}\|^2 \right)$$
$$\rightarrow \text{Min!} \tag{52}$$

$$f_x(\mathbf{b}, \mathbf{c}) := \|\tilde{\mathbf{x}}_\perp + \mathbf{A}_\perp \mathbf{b} + \mathbf{B}_\perp \mathbf{c}\|^2 + \rho \frac{g T^2}{2} \left(\|\mathbf{b}\|^2 + \|\mathbf{c}\|^2 \right)$$
$$\rightarrow \text{Min!} \tag{53}$$

This approach is well known as Tychonov regularization (Strang, 2007). The scalings involving Earth's acceleration g and the span T of the considered time interval have been introduced to provide the respective regularization term with the correct physical unit. The optimal choice for the regularization parameter is $\rho = 1$, which will be verified in the next section (compare Fig. 14): firstly, the smallest minimum of the objective function can be achieved for this choice. Secondly, the minimum is relatively insensitive to a variation of the parameter in a certain interval around 1 (see Fig. 14). Again, the minimization problem (52) is equivalent to an overdetermined system, namely to the system of $N + 6 + 9$ equations,

$$\begin{bmatrix} \mathbf{A}'_\perp & \mathbf{B}'_\perp \\ \rho g T \mathbf{I}_6 & \mathbf{O}_{6\times 9} \\ \mathbf{O}_{9\times 6} & \rho g T \mathbf{I}_9 \end{bmatrix} \begin{bmatrix} \mathbf{b} \\ \mathbf{c} \end{bmatrix} = - \begin{bmatrix} \tilde{\mathbf{v}}_\perp \\ \mathbf{0}_6 \\ \mathbf{0}_9 \end{bmatrix} \tag{54}$$

and analogously for (53),

$$\begin{bmatrix} \mathbf{A}_\perp & \mathbf{B}_\perp \\ \rho \frac{g T^2}{2} \mathbf{I}_6 & \mathbf{O}_{6\times 6} \\ \mathbf{O}_{9\times 6} & \rho \frac{g T^2}{2} \mathbf{I}_9 \end{bmatrix} \begin{bmatrix} \mathbf{b} \\ \mathbf{c} \end{bmatrix} = - \begin{bmatrix} \tilde{\mathbf{x}}_\perp \\ \mathbf{0}_6 \\ \mathbf{0}_9 \end{bmatrix} \tag{55}$$

Therein, $\mathbf{I}_6$ is the (6×6)-identity matrix, $\mathbf{O}_{9\times 6}$ the (9×6)-zero matrix, $\mathbf{0}_6 = \mathbf{O}_{6\times 1}$, etc.

5.2. Quantitative analysis based on in situ calibration

5.2.1. Determination of calibration parameters
The parameter vectors $\mathbf{b}$ and $\mathbf{c}$ of the accelerometer error model result from the postulate that the constraint condition is fulfilled in a least squares sense either at position level or at velocity level (Eqns (44) and (45), respectively). To this end, the overdetermined systems of equation (54) or (55) have to be solved. The input quantities entering this procedure are: $\mathbf{R}_n$, $^1\tilde{\mathbf{a}}_n$, $^0\tilde{\mathbf{v}}_n$ and $^0\tilde{\mathbf{x}}_n$. The tilde refers to values based on the laboratory calibration (prior to recalibration).

Applying the velocity constraint without considering the linear drift term involving $\mathbf{b}_1$, one obtains

$$\mathbf{b}_0^{(v)} = \begin{bmatrix} -0.086263 \\ 0.011683 \\ -0.006500 \end{bmatrix},$$

$$\mathbf{C}^{(v)} = \begin{bmatrix} -0.008369 & 0.025738 & -0.04306 \\ -0.010927 & 0.005685 & 0.039751 \\ 0.029010 & -0.086067 & 0.061000 \end{bmatrix}$$

whereas the position constraint yields

$$\mathbf{b}_0^{(x)} = \begin{bmatrix} -0.061926 \\ 0.023639 \\ 0.001839 \end{bmatrix},$$

$$\mathbf{C}^{(x)} = \begin{bmatrix} -0.004843 & -0.002775 & -0.027261 \\ -0.013881 & 0.028386 & 0.014610 \\ 0.015133 & -0.044731 & 0.056375 \end{bmatrix}$$

From a physical point of view, the two constraint conditions are expected to yield similar results. In fact, the values of corresponding parameters differ by less that $\pm 20\%$,

$$\delta \mathbf{b} = \begin{bmatrix} -0.158 \\ -0.078 \\ -0.054 \end{bmatrix}, \quad \delta \mathbf{c} = \begin{bmatrix} -0.017 & 0.133 & -0.074 \\ 0.014 & -0.106 & 0.118 \\ 0.065 & -0.194 & 0.022 \end{bmatrix}$$
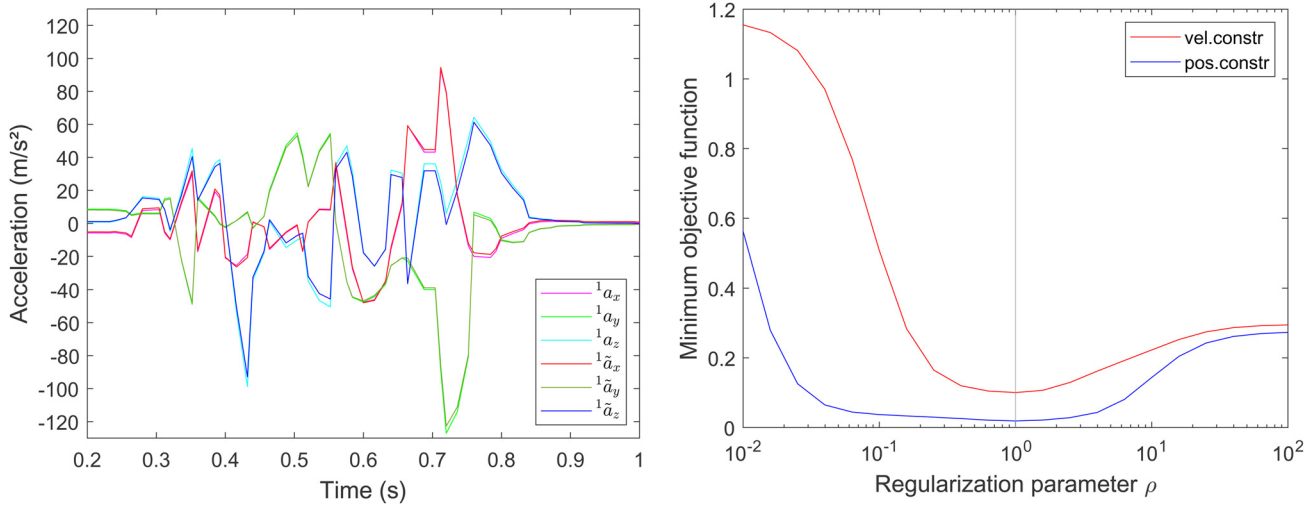
Figure 14. *Left:* Local acceleration components before (red/dark green/blue) and after (magenta/green/cyan) recalibration. *Right:* Obtained minima of the objective functions according to the minimization problems (52) and (53), respectively, in dependence of the regularization parameter ρ. Note that the minimum objective function can be considered as a measure for the violation of the constraint condition.

with the relative difference being defined as $\delta\mathbf{b} = (\mathbf{b}_0^{(v)} - \mathbf{b}_0^{(x)})/(\|\mathbf{b}_0^{(v)}\| + \|\mathbf{b}_0^{(x)}\|)$ and analogously for $\delta\mathbf{c}$. On a first glance, the impact of the recalibration on the acceleration components is small (see Fig. 14, left). Its impact on the recovered trajectories, however, is significant, as will be explicated in detail in the next section. The recalibration also effects the determination of the initial orientation $\mathbf{R}_0$ (Eqns (12)–(14)). This effect can be quantified by identifying the rotation vector $\delta\boldsymbol{\varphi}^{(x)}$ related to the rotation matrix $\delta\mathbf{R} = \mathbf{R}_{0,recal}\mathbf{R}_0^T$,

$$\delta\boldsymbol{\varphi}^{(x)} = \begin{bmatrix} -2.724° & 0.620° & -1.002° \end{bmatrix}^T$$

Thus, the observed inclination of the magnetic field changes according to

$$I_x = \bar{I} - \varphi_x^{(x)} \approx 61.191° + 2.724° \approx 63.92°$$

That is, the correction of the inclination tends in the right direction, though it is too large, such that $I_0 - I_x \approx -1.10°$ (instead of $+1.62°$ prior to recalibration). Now the absolute error goes below the standard deviation ($1.3°$). The given numbers refer to the position constraint. For the velocity constraint, the angular deviation is even more pronounced,

$$\delta\boldsymbol{\varphi}^{(v)} = \begin{bmatrix} -3.516° & 2.475° & -4.602° \end{bmatrix}^T$$

such that the error of the observed inclination becomes $I_0 - I_v \approx -1.89°$, which is even (absolutely) larger than the error prior to recalibration.

Concluding, the influence of the regularization parameter ρ entering the minimization problems (52) and (53), respectively, shall be investigated (see Fig. 14, right). For the velocity as well as for the position constraint, the smallest minimum of the objective function is achieved for $\rho = 1$. Moreover, the minimum is relatively insensitive to a variation of the parameter in a certain interval around 1. There is a pronounced interval of insensitivity for the position constraint ($5 \cdot 10^{-2} \lesssim \rho \lesssim 5$). This is a necessary condition for the regularization approach to be valid. For the velocity constraint, this interval is significantly smaller, which makes the corresponding results less robust. Note that the sensitivities of the minimum objective function with respect to a variation of the regularization parameter are scalar measures for the sensitivities of the position and velocity functions, $\mathbf{x}(t)$ and $\mathbf{v}(t)$, respectively.

Referring to the interval $5 \cdot 10^{-2} \le \rho \le 5$, the variation of the minimum objective function is in the range of ± 0.02. Correspondingly, the variation of the $\mathbf{x}(t)$ function is of the same order of magnitude ($\sim \pm 2\%$).

5.2.2. Constrained trajectory

The calibration parameters obtained from the two different types of constraint conditions (and an accelerometer error model (28) involving a constant bias but no drift) are subsequently used to recalibrate the accelerometer values, which, in turn, are applied to calculate new estimates of the sensor unit trajectory. In Figure 15, these results are compared to each other, to the original estimate of the trajectory according to standard calibration on the basis of laboratory data, and to the reference tube. According to the design of the method, the vertical projections of the constrained trajectories (right diagram in the figure) match the terrain line in an averaged sense. In contrast, dealing with the vertical projection (left diagram), the overall deviation of the constrained trajectories from the reference tube appears to become larger compared to their unconstrained counterpart. For a more detailed assessment of the new results it is beneficial to consider the position coordinates with respect to the slope coordinate system,

$$^sx = \mathbf{e}_x^s \cdot (\mathbf{x} - \mathbf{x}_0), \quad ^sy = \mathbf{e}_y^s \cdot (\mathbf{x} - \mathbf{x}_0), \quad ^sz = \mathbf{e}_y^s \cdot (\mathbf{x} - \mathbf{x}_0)$$

That is, ^sx (longitudinal coordinate) is the distance from the starting point of the sensor unit measured along the slope secant (Section 4.2.1); ^sy (lateral coordinate) and ^sz (transverse coordinate) are the normal distances from the slope secant measured in horizontal direction and in the slope normal direction, respectively. With other words, ^sx is approximately the travelling distance, ^sy and ^sz measure the deviation from the slope secant. Accordingly, Figure 16 shows the deviation of the estimated trajectories from the slope secant. The following conclusions can be drawn from the diagrams:

1. The acceleration phase ranging from $^sx = 0$ m to $^sx \approx 1$ m is accompanied by a small lateral movement in the order of 0.1 m.
2. The ballistic motion phase at the beginning of the sensor unit movement is clearly represented in the trajectory plot, where it appears in the shape of a ballistic parabola ranging from $^sx \approx 1$ m to $^sx \approx 21$ m (right diagram in Fig. 16).
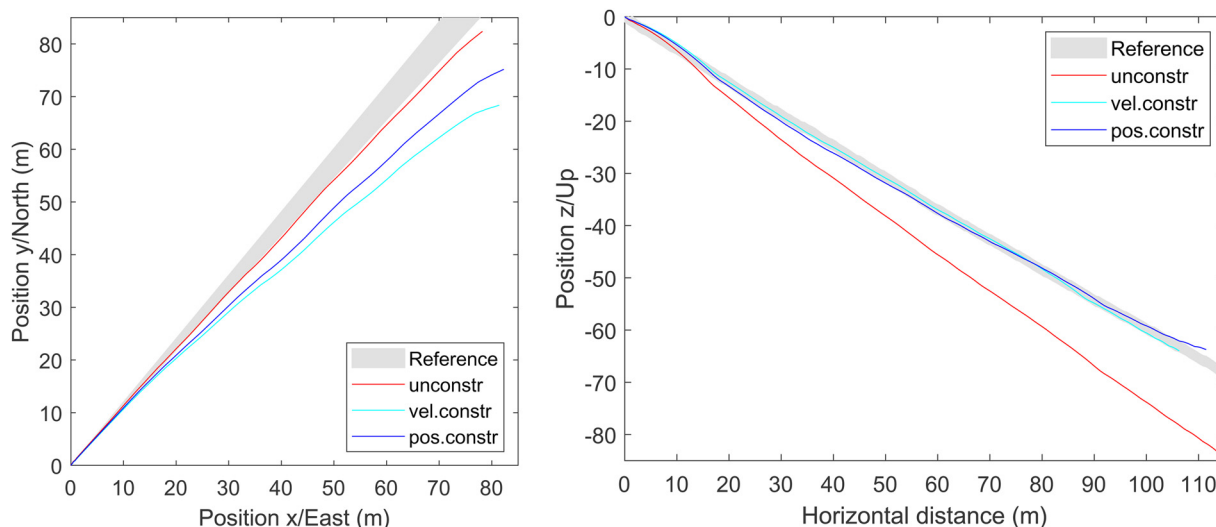
Figure 15. Sensor unit trajectories recovered from IMU data subjected to laboratory calibration (red) and to in situ calibration based on velocity (cyan) and position constraint (blue), respectively. The projections of the reference tube are shown in grey. *Left:* Top view, i.e. a normal projection onto a horizontal plane. *Right:* Vertical section, i.e. a normal projection onto a vertical plane passing through the slope secant.
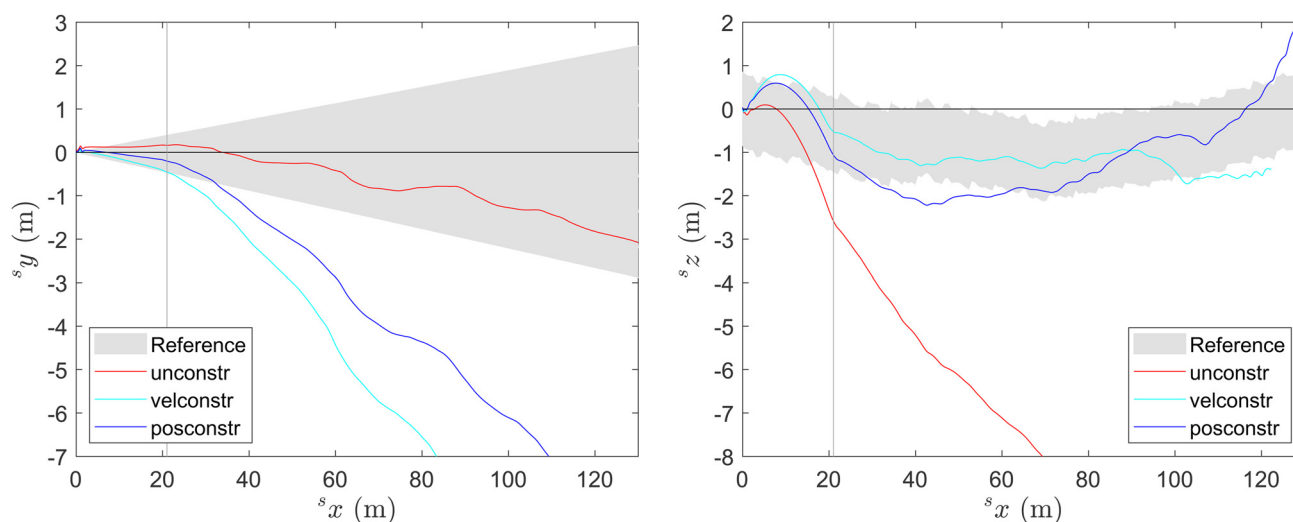

Figure 16. Estimates of the sensor unit trajectory drawn in the inclined *x-y* plane (i.e. approximately the terrain surface) of the slope coordinate system (*left*) and in the vertical *x-z* plane (*right*). The vertical grey lines indicates the end of the ballistic flight path. The horizontal lines passing through the origin refer to the slope secant. Correspondingly, the left and right diagrams show the lateral and transverse deviation from the slope secant. Note that the reference tube is derived from the measured terrain model and is therefore not aligned exactly with the slope secant.

3. The reliability of the unconstrained trajectory is poor, since the orientation of the ballistic parabola is not plausible. (A correct starting orientation of the trajectory is considered as a *necessary* condition for the reliability of a tracking procedure.)
4. The starting orientations of the constraint trajectories are within an acceptable range.
5. Each of the trajectories constrained in transverse direction suffers from a severe (basically quadratic) drift in the lateral direction (left diagram), which is to be expected, given the low sampling rate applied (compared to contemporary standards).
6. The transverse deviation from the slope line (right diagram) is of the same order of magnitude as the estimated accuracy of the reference tube until it starts to diverge close to the end of the processed time interval (corresponding to a travelling distance of $\approx$120 m).[13]

---

[13]A divergence can only be observed for the position constraint, where it appears just before the onset of data failure. Probably, a similar behaviour should be expected from the velocity constraint, but is masked by the data gap.
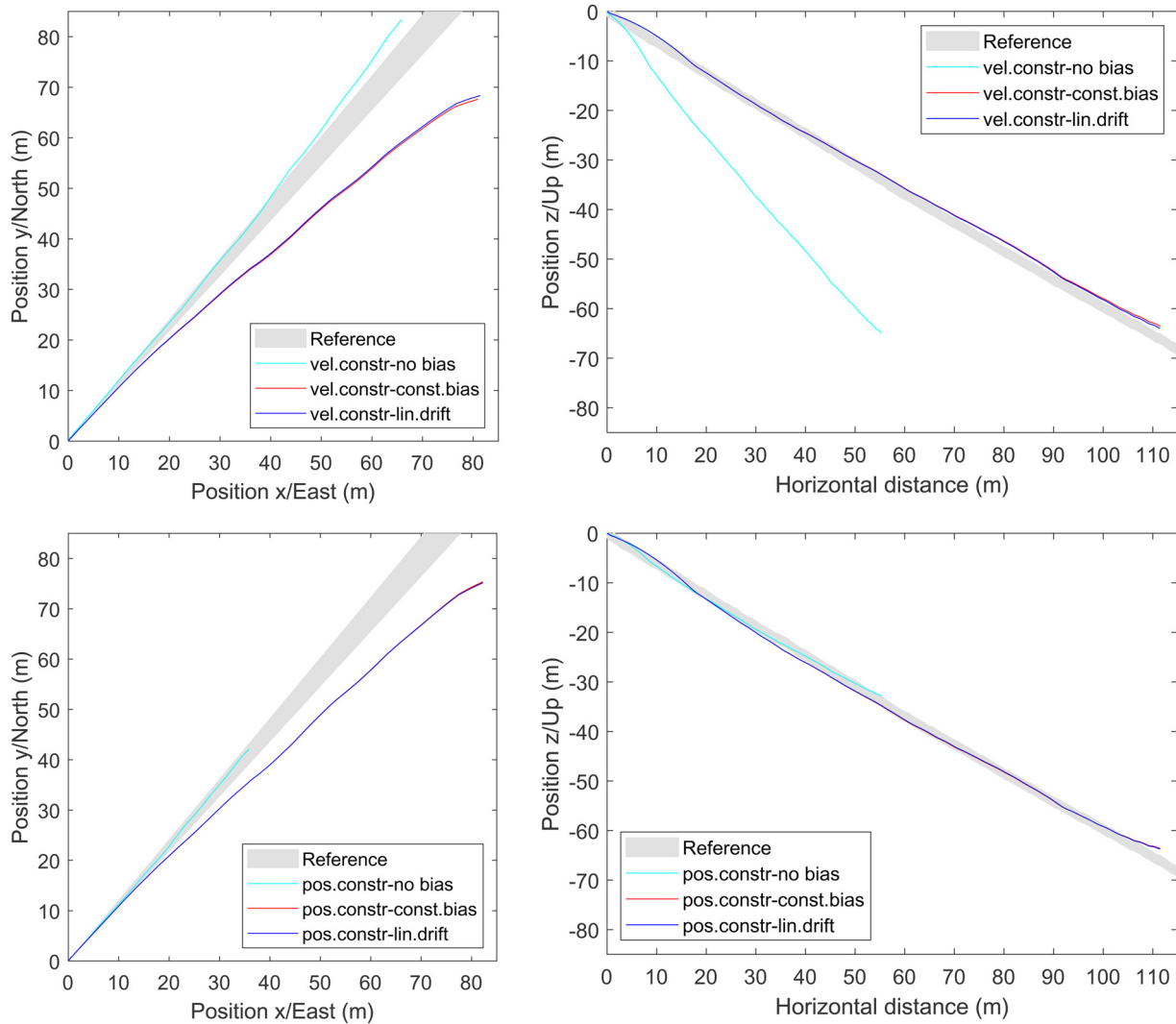
7. Based on the trajectory results, a clear preference for the position or the velocity constraint cannot be deduced. The explications of the previous section, however, assign a higher reliability to the position constraint.

The calculations have been repeated, once without considering any bias, i.e. $\mathbf{b}_0 = \mathbf{b}_0 = \mathbf{0}$ and once with all terms included in the error model (28), i.e. considering constant bias and linear drift and are referred to as

1. No bias: $^1\mathbf{a}_n = (\mathbf{I} + \mathbf{C})^1 \tilde{\mathbf{a}}_n$
2. Constant bias: $^1\mathbf{a}_n = (\mathbf{I} + \mathbf{C})^1 \tilde{\mathbf{a}}_n + g\mathbf{b}_0$
3. Linear drift: $^1\mathbf{a}_n = (\mathbf{I} + \mathbf{C})^1 \tilde{\mathbf{a}}_n + g\mathbf{b}_0 + g\tau_n\mathbf{b}_1$

The corresponding tracking results are summarized in Figure 17. It turns out that models (2) and (3) yield virtually identical results, whereas model (1) does not work properly. This observation holds for the velocity as well as for the position constraint. Clearly, approach (2) is to be preferred since approach (3) relies on a larger number of parameters without delivering better

Figure 17. Comparison of error models (1)–(3) for the velocity (*top*) and position constraint (*bottom*).

results. Thus, all position and velocity results presented in this section without an explicit reference to the error model rely on approach (2).

5.2.3. Translational velocities

The recovered translational velocity components are plotted in Figure 18. In the left diagram, the global components obtained before (cyan, green, magenta refer to global z, x, y components, respectively) and after recalibration (red, darkgreen, blue) are compared to each other. Apparently, the vertical velocity component ^0v_z is effected most by the recalibration. This is what has to be expected according to the nature of the constraint condition. The divergence of the results according to position and velocity constraints is less significant (solid vs. dotted lines). There is also a certain deviation in the evolution of the ^0v_y components, which reflects the drift observed in the horizontal projection of the trajectory and is thus considered as a result of accumulated noise with no physical significance. For a further interpretation of the velocity results it is again useful to consider the components with respect to the slope coordinate system (Section 4.2.1), i.e. $^s\mathbf{v} = \mathbf{Q}_s^{T\,0}\mathbf{v}$, which are plotted in the right diagram of Figure 18. Correspondingly, ^sv_x refers to the direction of the slope secant (longitudinal), ^sv_y, to the horizontal (lateral) direction and ^0v_z to the direction normal to the terrain (transverse). As expected, the ^sv_y values are relatively small. However, instead of simply oscillating around zero, they reveal the linear drift

mentioned before. The motion phases identified within the qualitative IMU data analysis are reflected by the velocity evolution:

1. Acceleration phase from $t \approx 0.25$ s to $t \approx 0.80$ s: a strong and progressive increase of the ^sv_x component occurs (Fig. 18, right).
2. Ballistic motion from $t \approx 0.80$ s to $t \approx 1.67$ s: horizontal components ^0v_x and ^0v_y are basically constant, while the vertical component $-^0v_z$ is linearly increasing according to Earth's acceleration (Fig. 18, left). The evolution of the transverse component ^sv_z indicates that a pronounced motion normal to the terrain surface occurs that changes from outward ($^sv_z > 0$) to inward ($^sv_z < 0$) orientation (Fig. 18, right).
3. Impact at $t = 1.67$ s: a sudden deceleration occurs in longitudinal ($\mathbf{e}_x^s$) as well as in transverse direction ($\mathbf{e}_z^s$), see the right diagram of Figure 18.
4. 'Steady flow' motion starting at $t \geq 1.67$ s: the motion is dominated by the longitudinal component ^sv_x. It is slowly decelerating and is superimposed by a basically random jerking (Fig. 18, right).

On the basis of supplementary Doppler radar measurements, the motion of the avalanche front has been determined. The observed signal is shown in the diagram in Figure 3, from which the range-time curve of the avalanche front can be deduced (as a step function), see also the right diagram of Figure 19. Accordingly, one single velocity value for each of the subsequent
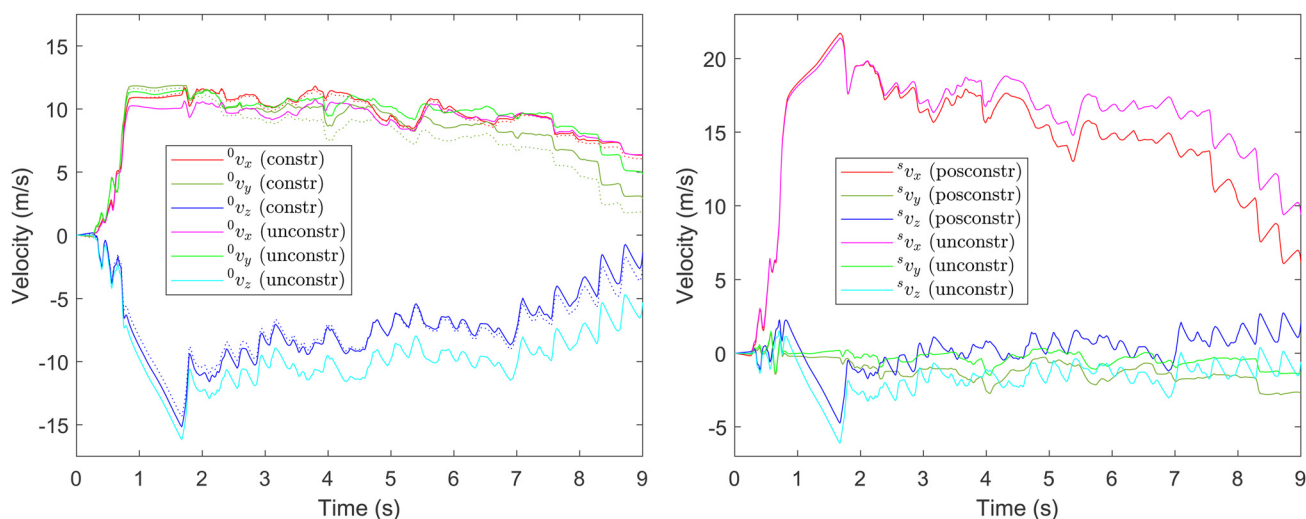
Figure 18. Translational velocity components vs. time. Global components (*left*) and components with respect to the slope frame (*right*). Comparison of results before and after recalibration. Solid lines refer to the position constraint, dotted lines to the velocity constraint.
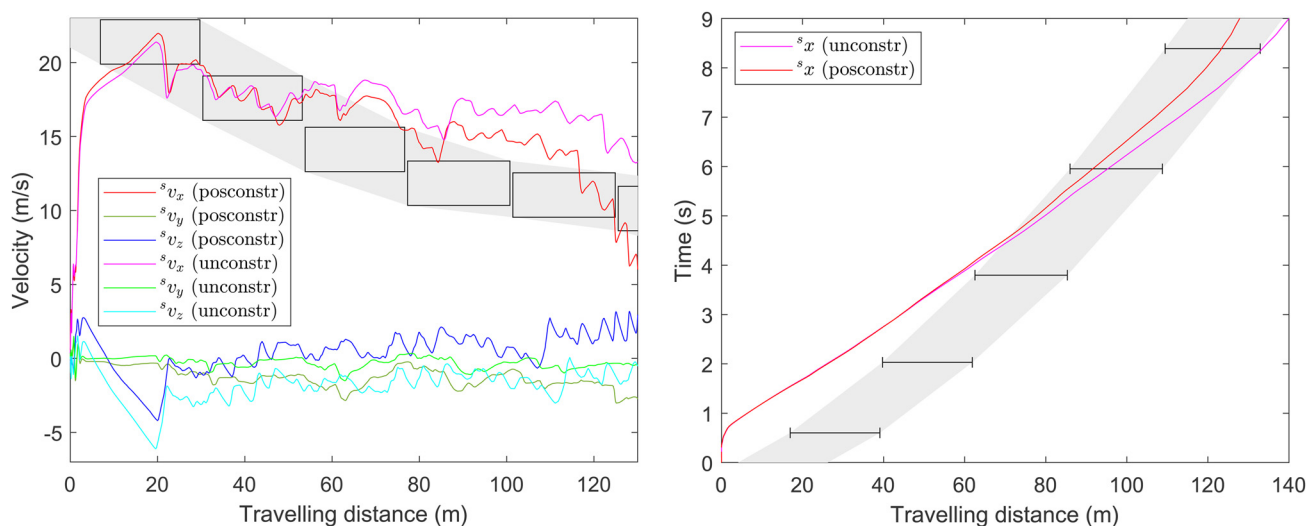

Figure 19. Translational velocity components with respect to the slope frame vs. travelling distance $^s x$ (*left*) and the corresponding path-time diagram (*right*). Both diagrams provide a comparison with the Doppler radar results (gray domains): velocities (*left*) and range-time diagram of the avalanche front (*right*) projected on the terrain. The horizontal span of the error boxes and bars refers to the length of each range gate (≈ 25 m). The vertical span of the error boxes refers to the uncertainty of the velocity evaluation ($\approx \pm 1.5$ m s^{-1}). Note that close to a travelling distance of 125 m (according to $t \approx 9$ s) the data corruption occurs.

range gates is determined. The span of the recovered sensor unit trajectory covers five entire range gates, which are represented by black framed error boxes in the left diagram of Figure 19. The length of each box corresponds to the length of the range gate (≈ 25 m, each) and the width is given by the estimated accuracy of the velocity evaluation ($\approx \pm 1.5$ m s^{-1}). For the representation in the diagram, position and length of each range gate as well as the measured velocity have been projected onto the slope secant.

From the velocity evolution displayed in the left diagram of Figure 19, it can be seen that the avalanche is in a decelerating phase already before the sensor unit is entrained. It takes the sensor unit 10–20 m to reach a velocity, which is similar to the one of the avalanche front (≈ 20 m s^{-1}), meaning that the sensor unit is necessarily several metres (definitely less than a 25 m range gate) behind the front at that instant. Subsequently, the sensor unit appears to move roughly at the same decelerating speed as the avalanche front. After a travelling distance of about 50 m, the

sensor unit velocity seems to decrease less than the frontal velocity, i.e. the sensor unit moves towards the front, which it appears to reach after a travelling distance of 70–100 m. From then on, the sensor unit is expected to remain close to the avalanche front for a while. This plausible scenario fits well with the data presented in both diagrams of Figure 19. The comparison of sensor unit and frontal velocities on the same range axis is justified by the observation that the maximum distance between the sensor unit and the avalanche front is significantly smaller than the length of a range gate. In addition, the diagram supports the conclusion that the tracking procedure prior to recalibration overestimates the longitudinal velocity significantly, whereas the ('constrained') velocity according to *in situ* calibration better fits to the radar data. After a travelling distance of about 120 m (just before the onset of data corruption), the constrained velocity drops below the radar velocity. This behaviour is assessed to be unphysical and to originate from the escalating lateral drift occurring close to the end of the processed time interval.

6. Discussion

A consistent assessment of the presented results is a delicate issue since they refer to a unique dataset, which has required specific methods of evaluation, in particular, the in situ approach for sensor calibration. Suitable reference data, which could be applied for a validation of these methods, are difficult to obtain. As discussed in Section 5.1, the method of in situ calibration essentially relies on a peculiarity of the observed sensor unit motion: a sufficiently good conditioning of the equation system determining the calibration parameters is only achieved, if the 'randomness' of the involved rotations is sufficiently high. Accordingly, it would be extremely laborious to design and conduct a reference experiment to obtain a proper dataset for the validation procedure. The test device would have to reproduce a suitable type of rotational motion superimposed to a long-range translational motion. Moreover, the algorithms applied in the paper essentially rely on magnetometer data. To reproduce the characteristics of the field experiment, one would have to create a reference motion without inducing any (electro-)magnetic disturbances in the sensors. Under these circumstances, an automated guided motion can hardly be achieved. Simple rolling outdoors would not meet the requirements concerning the character of the rotational motion. Rotating by hand might be a possibility, however monitoring the rotational motion would require an additional measurement system, which would have to be validated itself.

Referring to these difficulties, we suggest to clearly distinguish between a conceptual validation on the one hand and an assessment of accuracy on the other. Specifically, our conceptual validation refers to the following aspects: the reliability of angular orientations is assessed by the degree of constancy of the global magnetic field components and by the reproducibility of the inclination. The conceptual integrity of the recovered trajectory is deduced form the correctly reproduced orientation of the initial motion sequence. Finally, the recovered velocity evolution is compared to the velocity of the avalanche front, which reveals a good coincidence immediately after the acceleration phase and yields a plausible interpretation of the sensor unit motion relatively to the avalanche front thereafter. Strictly speaking, the quoted criteria are *necessary* (but not sufficient) conditions for the integrity of the results. Arguments to further support the results are of rather qualitative nature: a closer investigation of the evolution of angular velocities and orientation in Section 4.2.2 reveals a plausible characteristic of the initial rotation sequence, which would not be expected if there is a relevant error in the angular orientations. A similar argument holds for the translational velocity components, treated in Section 5.2.3. Referring to a comment of one of the reviewers, it is mentioned that the terrain surface cannot be taken as a reference for the trajectory, since the related information is already essentially used for the in situ calibration.

Dealing with the question of accuracy, it has to be stated that the achieved long-term accuracy of the tracking procedure is rather poor. Owing to the well-discussed shortcomings of the data acquisition and, in particular, of the low sampling rate, this fits well to the expectations. It is emphasized that the heavy drift observed in the horizontal projection of the trajectory is *not* considered to conflict with the conceptual validation, but is rather considered a matter of low accuracy (due to the well-discussed reasons). Unfortunately, the well-known end position of the sensor unit can neither be applied to reduce the positioning error nor to provide for an assessment of the accuracy of the method, since we don't see a realistic chance to bridge the data gap (Section 3), which would allow to link the information about the initial and the final motion sequence.

A particularly interesting aspect of the recovered motion is related to the ballistic flight phases, reflected by a smooth parabolic trajectory, which proves that, in principle, the method is capable of quantitatively reproducing a transverse motion, i.e. a motion perpendicular to the terrain. In view of avalanche dynamics, this aspect is of particular interest, since no other experimental method for the observation of through-the-depth motion in an avalanche is known so far. Referring to a comment of one reviewer, it is noted that the observed transverse movement is, most likely, not directly related to the snow movement, since the sensor unit appears to be detached from the avalanche body. From a more fundamental point of view, the observation supports the underlying assumption that the constraint is not too restrictive, in the sense that it is capable of circumventing a numerical drift perpendicular to the terrain without suppressing physical motion in the same direction. This results, however, are of preliminary character until they will be reproduced by further experiments with a technologically advanced sensor equipment.

According to the nature of the tracking procedure, velocity results are more accurate than position results. At the present status of data evaluation, it appears that the information relevant for avalanche dynamics can be extracted from the recovered velocity evolution without further reference to the (less reliable) trajectory. This involves the motion of the sensor unit relatively to the avalanche front, which – in the present experiment – cannot be seen from other observations and – potentially – the detection and quantification of through-the-depth motion within the avalanche body, as well as the comparability with the results of alternative experimental methods such as radar velocity measurements, GNSS and radio ranging measurements, and, in particular, of numerical models.

7. Conclusion and outlook

The outcome of this paper is twofold: primarily, a real scale avalanche experiment is qualitatively and quantitatively analysed from different perspectives, involving in-flow measurements of inertial data, radar observations and GNSS positioning. To extract a maximum of information from the measurements, a number of ad hoc approaches were necessary to overcome several shortcomings associated with the lack of any in-field experience with the measurement set-up. From this, a secondary motivation arose, which gave rise to the development of a bundle of numerical methods for the processing of the specific inertial motion data.

It is demonstrated in principle that the applied sensor system is suited for the acquisition of in-flow data, which can be used for qualitative and quantitative motion analysis. The qualitative data analysis allows to clearly distinguish different flow phases of the sensor unit: rapid initial acceleration when being entrained at the avalanche front, steady flow movement superimposed with random jerks and short ballistic motion phases when being transported by the avalanche body, and rolling on the surface of the resting snow cover after being released from the bulk of moving snow.

The quantitative data analysis provides estimates of the evolution of the angular orientation, translational and angular velocity, as well as the trajectory of the sensor unit transported by the avalanche. To obtain plausible positioning results, a soft constraint condition is applied to recover the trajectory along the terrain surface. This approach is interpreted as a method of calibration, by which means the parameters of the accelerometer error model are determined such that the constraint condition is fulfilled in an averaged sense. The procedure is based solely on the data recorded in the course of the experiment. To account for this, the concept of in situ calibration is introduced. The constraint condition can be posed at a velocity level as well as at a position level. It turns out that both approaches yield similar results

concerning position and translational velocity data. A detailed assessment regarding the numerical stability of the method suggests to prefer the position level approach.

Experiences gained from the single experiment revealed the need for further, repeated measurement campaigns with an advanced hardware. Such experiments have most recently highlighted the potential of state-of-the-art GNSS to track particle motion in snow avalanches (Neuhauser and others, 2023). As a next step, high-resolution motion tracking requires a fusion of inertial and GNSS data, where conventional methods of state estimation may benefit from the in situ calibration approach of the present work.

References

Aggarwal P, Syed Z, Niu X and El-Sheimy N (2008) A standard testing and calibration procedure for low cost MEMS inertial sensors and units. *The Journal of Navigation* **61**, 323–336. doi: 10.1017/S0373463307004560

Bartelt P and McArdell B (2009) Instruments and methods: granulometric investigations of snow avalanches. *Journal of Glaciology* **55**(193), 829–833. doi: 10.3189/002214309790152384

Björck A (1996) *Numerical Methods for Least Squares Problems*. SIAM, Philadelphia.

Canadian Avalanche Association (2016) *Observation guidelines and recording standards for weather snowpack and avalanches*. Technical report, Canadian Avalanche Association, Revelstoke, BC, Canada.

Caviezel A and 9 others (2019) Reconstruction of four-dimensional rockfall trajectories using remote sensing and rock-based accelerometers and gyroscopes. *Earth Surface Dynamics* **7**(1), 199–210. doi: 10.5194/esurf-7-199-2019

Caviezel A and 9 others (2021) The relevance of rock shape over mass – implications for rockfall hazard assessments. *Nature Communications* **12**(1), 1–9. doi: 10.1038/s41467-021-25794-y

Crassidis JL, Markley FL and Cheng Y (2007) Survey of nonlinear attitude estimation methods. *Journal of Guidance, Control, and Dynamics* **30**(1), 12–28. doi: 10.2514/1.22452

De Quervain R (1981) *Avalanche Atlas*. UNESCO, Paris.

Dost JB, Gronz O, Casper MC and Krein A (2020) The potential of smartstone probes in landslide experiments: how to read motion data. *Natural Hazards and Earth System Sciences* **20**(12), 3501–3519. doi: 10.5194/nhess-20-3501-2020

Faug T (2015) Depth-averaged analytic solutions for free-surface granular flows impacting rigid walls down inclines. *Physical Review E* **92**(6), 062310. doi: 10.1103/PhysRevE.92.062310

Faug T, Turnbull B and Gauer P (2018) Looking beyond the powder/dense flow avalanche dichotomy. *Journal of Geophysical Research: Earth Surface* **123**(6), 1183–1186.

Fischer JT and Rammer L (2010) An introduction to inflow avalanche dynamics measurements using the SNOWBALL device. In *International Snow Science Workshop 2010, Squaw Valley, California, USA*.

Fischer JT, Fromm R, Gauer P and Sovilla B (2014) Evaluation of probabilistic snow avalanche simulation ensembles with Doppler radar observations.

Cold Regions Science and Technology **97**, 151–158. doi: 10.1016/j.coldregions.2013.09.011

Fischer JT, Kaitna R, Heil K and Reiweger I (2018) The heat of the flow: thermal equilibrium in gravitational mass flows. *Geophysical Research Letters* **45**(20), 11219–11226. doi: 10.1029/2018GL079585

Gauer P and Kristensen K (2016) Four decades of observations from NGI's full-scale avalanche test site Ryggfonn – summary of experimental results. *Cold Regions Science and Technology* **125**, 162–176. doi: 10.1016/j.coldregions.2016.02.009

Gauer P and 5 others (2007) On pulsed Doppler radar measurements of avalanches and their implication to avalanche dynamics. *Cold Regions Science and Technology* **50**, 55–71. doi: 10.1016/j.coldregions.2007.03.009

Groves P (2008) *Principles of GNSS, Inertial, and Multisensor Integrated Navigation Systems*, GNSS Technology and Applications Series. Artech House, Boston, London. ISBN 9781580532556.

Köhler A and 5 others (2018a) Cold-to-warm flow regime transition in snow avalanches. *The Cryosphere* **12**(12), 3759–3774. doi: 10.5194/tc-12-3759-2018

Köhler A, McElwaine J and Sovilla B (2018b) GEODAR data and the flow regimes of snow avalanches. *Journal of Geophysical Research: Earth Surface* **123**(6), 1272–1294. doi: 10.1002/jgrf.v123.6

Kyburz M, Sovilla B, Gaume J and Ancey C (2022a) Physics-based estimates of drag coefficients for the impact pressure calculation of dense snow avalanches. *Engineering Structures* **254**, 113478. doi: 10.1016/j.engstruct.2021.113478

Kyburz ML, Sovilla B, Gaume J and Ancey C (2022b) The concept of the mobilized domain: how it can explain and predict the forces exerted by a cohesive granular avalanche on an obstacle. *Granular Matter* **24**(2), 1–17. doi: 10.1007/s10035-021-01196-1

Madgwick SOH, Harrison AJL and Vaidyanathan R (2011) Estimation of IMU and MARG orientation using a gradient descent algorithm. *IEEE International Conference on Rehabilitation Robotics*, IEEE, Zürich.

Neuhauser M, Koehler A, Neurauter R, Adams M and Fischer J-T (2023) Particle trajectories, velocities, accelerations and rotation rates in snow avalanches. *Annals of Glaciology* 1–18. doi: 10.1017/aog.2023.69

Neurauter R and Gerstmayr J (2022) A novel motion-reconstruction method for inertial sensors with constraints. *Multibody System Dynamics* **57**(2), 181–209. doi: 10.1007/s11044-022-09863-8

Noël F and 5 others (2022) Rockfall trajectory reconstruction: a flexible method utilizing video footage and high-resolution terrain models. *Earth Surface Dynamics* **10**(6), 1141–1164. doi: 10.5194/esurf-10-1141-2022

Rammer L, Kern MA, Gruber U and Tiefenbacher F (2007) Comparison of avalanche-velocity measurements by means of pulsed Doppler radar, continuous wave radar and optical methods. *Cold Regions Science and Technology* **50**, 35–54. doi: 10.1016/j.coldregions.2007.03.014

Renaudin V, Afzal M and Lachapelle G (2010) Complete triaxis magnetometer calibration in the magnetic domain. *Journal of Sensors*. doi: 10.1155/2010/967245

Schnegg PA (1998) A procedure for modelling spatiotemporal variations of the geomagnetic field-example of the 1998 model for Switzerland. *Revista Geofísica* **48**(48), 133–140.

Schwartz R and Lindau A (2003) Das europäische Gravitationszonenkonzept nach WELMEC für eichpflichtige Waagen. *PTB-Mitteilungen* **113**, 35–42.

Simon D (2006) *Optimal State Estimation: Kalman, H Infinity, and Nonlinear Approaches*. John Wiley & Sons, Hoboken, New Jersey.

Sovilla B, McElwaine J and Louge M (2014) The structure of powder snow avalanches. *Comptes Rendus Physique* **16**(1), 97–104.

Sovilla B and 5 others (2016) Gravitational wet-avalanche pressure on pylonlike structures. *Cold Regions Science and Technology* **126**, 66–75. doi: 10.1016/j.coldregions.2016.03.002

Stančin S and Tomažič S (2014) Time- and computation-efficient calibration of MEMS 3D accelerometers and gyroscopes. *Sensors* **14**, 14885–14915. doi: 10.3390/s140814885

Steinkogler W, Gaume J, Löwe H, Sovilla B and Lehning M (2015a) Granulation of snow: from tumbler experiments to discrete element simulations. *Journal of Geophysical Research: Earth Surface* **120**(6), 1107–1126. doi: 10.1002/2014JF003294

Steinkogler W, Sovilla B and Lehning M (2015b) Thermal energy in dry snow avalanches. *The Cryosphere* **9**(5), 1819–1830. doi: 10.5194/tc-9-1819-2015

Strang G (2007) Computational science and engineering. *Optimization* **551**(563), 571–586.

Titterton D and Weston J (2004) *Strapdown Inertial Navigation Technology.* Electromagnetics and Radar Series, Institution of Engineering and Technology, United Kingdom.

Vilajosana I, Llosa J, Schaefer M, Surinach E and Vilajosana X (2011) Wireless sensors as a tool to explore avalanche internal dynamics: experiments at the Weissflühjoch snow chute. *Cold Regions Science and Technology* **65**(2), 242–250. doi: 10.1016/j.coldregions.2010.09.011

Wittenburg J (2008) *Dynamics of Multibody Systems.* Springer, Berlin, Heidelberg, New York.

Yun X, Bachmann ER and McGhee RB (2008) A simplified quaternion-based algorithm for orientation estimation from earth gravity and magnetic field measurements. *IEEE Transactions on Instrumentation and Measurement* **57** (3), 638–650. doi: 10.1109/TIM.2007.911646

Appendix A. Sensor calibration

It is a certain drawback of the present work that a proper calibration of IMU sensors has not been performed in temporal and spatial proximity of the field measurements. As it is generally the case for any measurement process, the IMU raw data are corrupted by systematic as well as stochastic sources of error. The former can be largely eliminated by standard methods of IMU sensor calibration. Assuming that the systematic errors are composed of a constant misalignment of sensor axes, constant scaling errors and constant offsets, linear calibration equations are obtained of the form

$$\mathbf{a}(t) = \mathbf{A} \cdot \tilde{\mathbf{a}}(t) + \mathbf{b} \qquad (A.1)$$

Therein, $\tilde{\mathbf{a}} = [\tilde{a}_x \; \tilde{a}_y \; \tilde{a}_z]$ is the vector of measured acceleration components at a given time t and $\mathbf{x}$ its improved counterpart, $\mathbf{A}$ the 3×3 calibration matrix and $\mathbf{b}$ the bias vector. Analogous error models are assumed for angular velocity sensors (gyrometers) and magnetometers. The calibration parameters (components of $\mathbf{A}$ and $\mathbf{b}$) are determined from reference measurements: for the accelerometer calibration, earth's acceleration is taken as a reference and is measured utilizing several different orientations of the sensor triad. While the magnitude of the true acceleration is constant, the magnitude of the measured acceleration will (slightly) differ from one orientation to another. An optimization procedure is applied to determine the calibration parameters such that the deviation from the true magnitude is minimum for all considered orientations in a least squares sense. Details on the underlying numerical procedure can be found in, e.g. Aggarwal and others (2008) and Stančin and Tomažič (2014). Such reference measurements have been performed in 2018, i.e. about 5 years after recording the field data at the Flüela Pass. Results are shown at the top of Figure 20 where raw data as well as calibrated data are drawn.

The calibration of gyrometers is performed on the basis of a reference motion generated by an industrial robot Stäubli TX2-90L. It can be seen from Figure 20 (bottom) that the quality of the gyrometer data is high even before the calibration, such that the effect of the calibration is marginal (but existent).

In the case of magnetometer calibration, a different strategy is pursued which is described in Renaudin and others (2010). The magnetometer data, and thus a reliable calibration of sensors, are crucial for the correct determination of angular orientation. The particular advantage of the chosen approach is that it allows to perform the calibration on the basis of the field data. This has become necessary since it turned out that the calibration of 2018, having been performed under laboratory conditions, is not valid for the field data of 2013, which can be seen from the bottom-right diagram of Figure 21: the avalanche data, subjected to the laboratory calibration, do not fit to the sphere, meaning that the magnitude of the measured magnetic field is not constant while the sensors are rotating.

The idea of the calibration procedure is to record a time series of magnetic field vectors ${}^1\mathbf{B}(t_n) = [\, {}^1B_x(t_n) \; {}^1B_y(t_n) \; {}^1B_z(t_n) \,]^T$ while rotating the sensor triad in a more or less arbitrary way. At the absence of (electro-)magnetic disturbances and assuming that the ${}^1B_i$ are ideal measurements, the tips of vectors ${}^1\mathbf{B}$ lie on a sphere with a radius that corresponds to the strength of Earth's magnetic field ($\approx$0.48 Gs). In the case of real measurements, this sphere shifts (hard iron distortion), deforms (soft iron distortion) and is superimposed by a basically random noise. Assuming that the transformation composed of a deformation and a shift is linear and constant in time, the deformed surface is an ellipsoid, and calibration equation (A.1) again applies. The calibration parameters, i.e. the components of the corresponding calibration matrix and bias vector, are obtained by fitting an ellipsoid to the measured data points. This procedure works best if the data points are uniformly distributed over
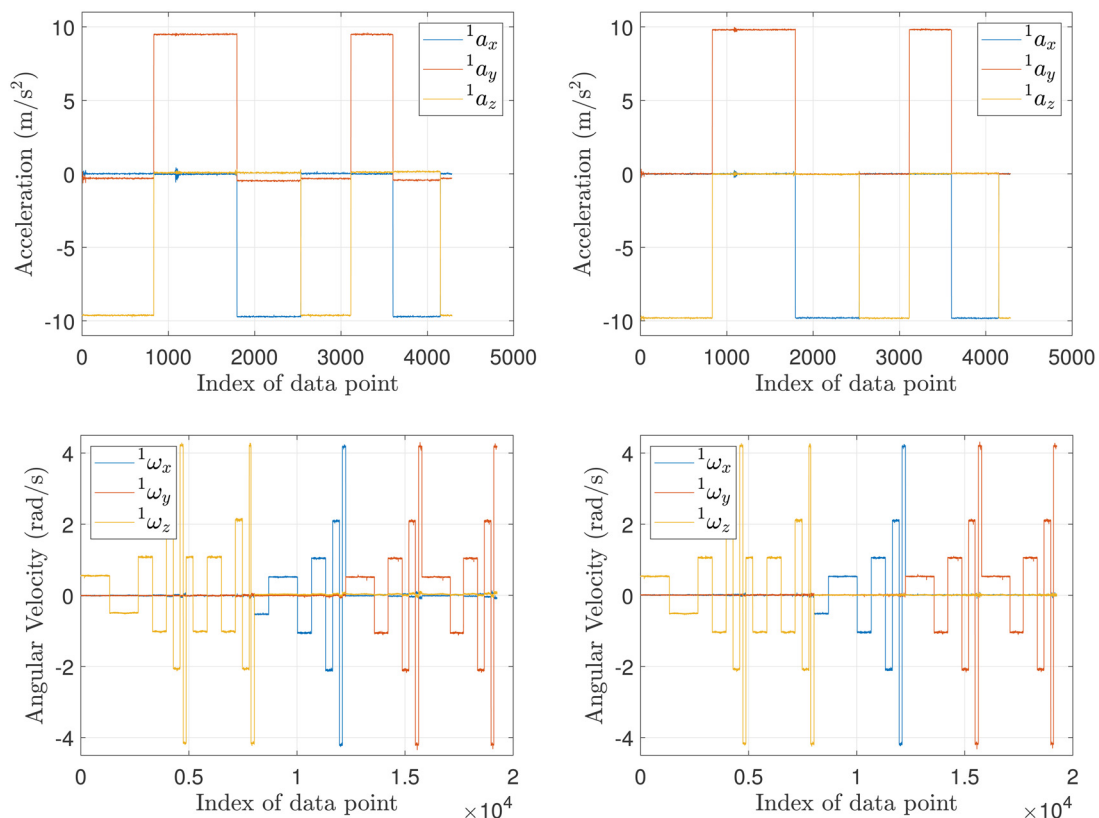

Figure 20. Laboratory calibration of accelerometers (top) and gyrometers (bottom): Uncalibrated (left) versus calibrated data (right). While the effect of calibration is apparent in the case accelerometers, it is marginal in the case of gyrometers.
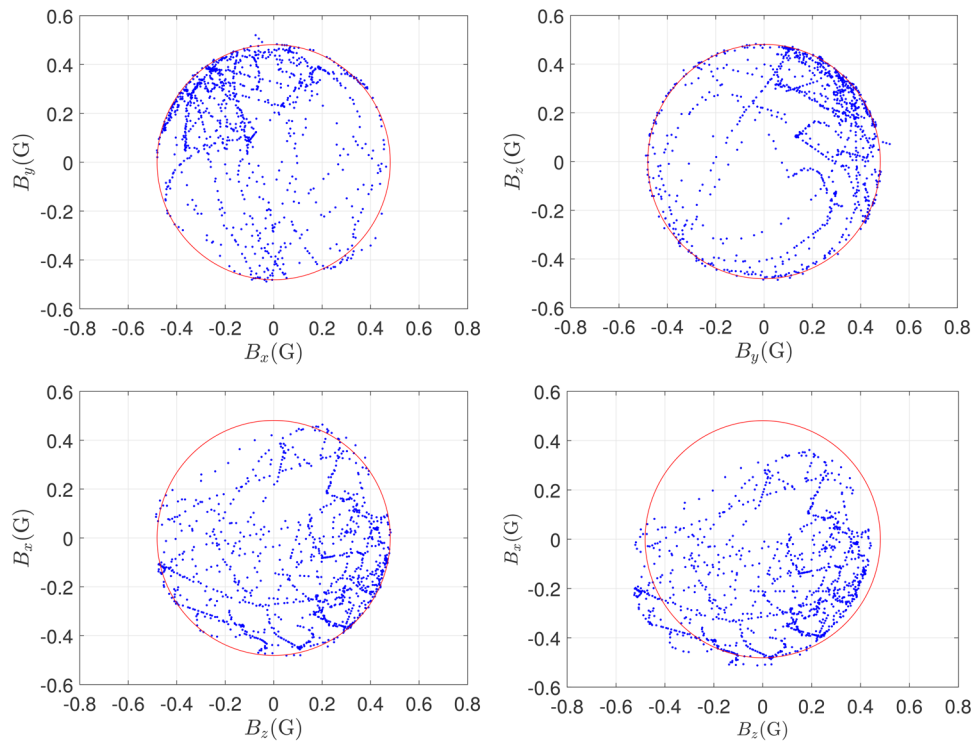
Figure 21. Top-left, top-right, bottom-left: Magnetic field data recorded in the course of the 2013 Flüela experiment subjected to in situ calibration. Bottom-right: The same data subjected to laboratory calibration of 2018.

the sphere/ellipsoid. This can be achieved to a certain degree in the course of laboratory calibration.[14] In the present case of in situ calibration, the data points reflect the actual rotational motion of the sensor in the course of the Flüela experiment: as can be expected, their distribution is by far not uniform. It turns out, however, that this kind of distribution is appropriate to achieve a sufficient accuracy of the calibration:

From what has been said before it can be deduced that the quality of the calibration can be assessed by the degree of non-constancy of $\|{}^1\mathbf{B}(t)\|$ or by the size of the deviation of the dataset from an ideal sphere. The latter criterion is even more significant, since the spread of the data is also apparent in the corresponding diagram. Dealing with the Flüela data, the bottom-right diagram in Figure 21 demonstrates the situation according to the laboratory calibration: the deviation from spherical shape is apparent, which implies that the laboratory calibration is not consistent with the in-field data. After recalibration on the basis of the in-field data (in situ calibration), the deviation is largely reduced and dominated by basically random noise (bottom-left diagram), although the distribution of the data point is not uniform. The diagrams at the top of the figure demonstrate the same aspect but with respect to different coordinate sections. Concluding, the quality of the achieved recalibration is assessed as adequate in the sense that the low-frequency variation of $\|{}^1\mathbf{B}(t)\|$ is smaller than the super-imposed random noise magnitude, which can be seen from the diagrams.

Appendix B. Replacement of deficient gyrometer data

The Flüela IMU data come along with the problem that the observed angular velocities have occasionally exceeded the measurement range of the gyroscopes ($\pm\,300°/\mathrm{s}^{-1}$, nominally). At several instances, only two out of the three angular velocity components ${}^1\omega_1$, ${}^1\omega_2$, ${}^1\omega_3$ are available (Fig. 6). However, the missing component(s) can be recovered with the help of the magnetometer data, as long as there is at least one component available. The corresponding procedure, which has been used in the present work, is described in the following.

The three magnetometers measure the components ${}^1B_k$ of earth's magnetic field $\mathbf{B}$ with respect to the corotational sensor coordinate system ($\mathbf{e}_1^1$, $\mathbf{e}_2^1$, $\mathbf{e}_3^1$).

That is,

$$
{}^1B_k = {}^1\mathbf{e}_k \cdot \mathbf{B} \tag{B.1}
$$

Denoting the effective angular velocity vector by $\boldsymbol{\omega}^\star$ (to be distinguished from the measured one), one has $\dot{\mathbf{e}}_k^1 = \boldsymbol{\omega} \times \mathbf{e}_k^1$ (Wittenburg, 2008). Since $\mathbf{B}$ is constant,

$$
{}^1\dot{B}_k = (\boldsymbol{\omega}^\star \times \mathbf{e}_k^1) \cdot \mathbf{B} = \mathbf{e}_k^1 \cdot (\mathbf{B} \times \boldsymbol{\omega}^\star) = \mathbf{e}_k^1 \cdot \tilde{\mathbf{B}} \cdot \boldsymbol{\omega}^\star \tag{B.2}
$$

with $\tilde{\mathbf{B}}$ being the skew-symmetric matrix related to the vector $\mathbf{B}$. Equation (B.2), for $k = 1,\ 2,\ 3$, can be interpreted as a system of equations constraining the ${}^1\omega_k$.

Unfortunately, this system is underdetermined, which has a simple geometric reason: a rotation about the direction of the $\mathbf{B}$ vector does *not* affect the corotational coordinates ${}^1B_k$. However, the three equations (B.2) can be enriched by obvious additional equations to obtain an overdetermined system

$$
\begin{bmatrix}
0 & -{}^1\hat{B}_3 & {}^1\hat{B}_2 \\
{}^1\hat{B}_3 & 0 & -{}^1\hat{B}_1 \\
-{}^1\hat{B}_2 & {}^1\hat{B}_1 & 0 \\
1 & 0 & 0 \\
0 & 1 & 0 \\
0 & 0 & 1
\end{bmatrix}
\cdot
\begin{bmatrix}
{}^1\omega_1^* \\
{}^1\omega_2^* \\
{}^1\omega_3^*
\end{bmatrix}
=
\begin{bmatrix}
{}^1\dot{\hat{B}}_1 \\
{}^1\dot{\hat{B}}_2 \\
{}^1\dot{\hat{B}}_3 \\
{}^1\omega_1 \\
{}^1\omega_2 \\
{}^1\omega_3
\end{bmatrix}
\tag{B.3}
$$

To ensure a favourable conditioning of system (B.3), the components of the magnetic field have been normalized, i.e. ${}^1\hat{B}_k = {}^1B_k/\|\mathbf{B}\|$, where $\|\mathbf{B}\|$ is the constant magnitude of earth's magnetic field. If, at a certain instant, one or two of the measured angular rates ${}^1\omega_k$ is/are missing, the respective line(s) in system (B.3) is/are simply eliminated. The time derivatives of the normalized magnetic field components at time step n, ${}^1\dot{\hat{\mathbf{B}}}_n = [\,{}^1\dot{\hat{B}}_1^{(n)} \quad {}^1\dot{\hat{B}}_2^{(n)} \quad {}^1\dot{\hat{B}}_3^{(n)}\,]^T$, are estimated by means of the symmetric difference quotient

$$
{}^1\dot{\hat{\mathbf{B}}}_n \approx \frac{{}^1\hat{\mathbf{B}}_{n+1} - {}^1\hat{\mathbf{B}}_{n-1}}{t_{n+1} - t_{n-1}} \tag{B.4}
$$

[14]In the present case, the assembled sensor unit of spherical shape, supported by the circular edge of an open bowl, has been slowly rotated by hand in random directions.

for $n \geq 1$. For the first ($n = 0$) and the last time step the right and the left difference quotients, respectively, are used instead.